Evolution of Spatially Entangled Photons Beyond Standard Approximations

Christian Howard

Thesis submitted to the University of Ottawa in partial fulfillment of the requirements for the degree of Master of Science, Physics: Concentration in Quantum Science

Department of Physics
Faculty of Science
University of Ottawa

Thesis Supervisor: Dr. Ebrahim Karimi

Abstract

Spontaneous parametric down-conversion (SPDC) is one of the most important sources of entangled photons in quantum optics and underpins a wide range of applications in quantum communication, quantum imaging, quantum sensing, and photonic quantum information processing. In this nonlinear optical process, a pump photon is converted into a pair of lower-energy photons that exhibit strong correlations in multiple degrees of freedom. While the generation of photon pairs is governed by energy and momentum conservation, the resulting biphoton state possesses a rich spatial structure whose properties are determined by the interplay among the pump field, the nonlinear medium, and subsequent propagation. This thesis investigates the spatial properties of entangled photon pairs generated through SPDC, focusing on the evolution of their correlations in the near field and on the behavior of orbital-angular-momentum (OAM) entangled states under tight focusing conditions. A common theme throughout this work is the examination of physical effects that emerge when the full biphoton wavefunction is retained rather than reduced through the simplifying approximations often employed in theoretical treatments. The principal contribution of this thesis concerns the near-field propagation of SPDC photon pairs. The spatial correlations of SPDC-generated photons are commonly analyzed within the thin-crystal approximation, where the biphoton wavefunction is assumed to factorize into independent functions of the sum and difference coordinates. We demonstrate that birefringence-induced transverse walk-off breaks this factorization and introduces an intrinsic coupling between these coordinates. More importantly, this coupling survives free-space propagation and remains observable even for crystals that nominally satisfy the thin-crystal condition. As a result, the joint spatial correlations develop a characteristic tapering near the crystal image plane that cannot be captured by conventional factorized models. Numerical simulations and experimental measurements are found to be in excellent agreement, revealing a previously overlooked feature of SPDC and providing a more complete description of photon-pair generation and propagation in birefringent nonlinear media. The second part of the thesis explores the propagation of OAM-entangled photon pairs beyond the paraxial regime. While OAM correlations are typically studied under weak-focusing conditions, many emerging quantum technologies require structured quantum states to be manipulated in highly confined optical systems. We show that tight focusing modifies the OAM correlation spectrum, leading to a broadening of the accessible mode distribution.

This broadening exhibits distinct transverse and longitudinal characteristics and arises from the emergence of nonparaxial field components absent in conventional scalar descriptions. These results provide new insight into the behavior of structured quantum light in strongly focused optical fields and establish a framework for understanding OAM entanglement beyond the paraxial approximation. Together, the results presented in this thesis reveal previously unexplored aspects of the structure and propagation of entangled photon pairs. By moving beyond widely used approximations, this work uncovers physical effects that influence the generation, evolution, and measurement of spatially entangled states, with implications for quantum imaging, high-dimensional quantum communication, and the broader development of structured-light-based quantum technologies.

Acknowledgements

I would like to begin by making several acknowledgments. First, I want to extend a massive thank you to Dr. Ebrahim Karimi for supporting me throughout my studies over the last two years and giving me the wonderful opportunity to study and work with him as a part of the SQO group. I have made many happy memories over the last two years that I will certainly keep with me for many years to come. I would also like to thank Dr. Alessio D'Errico for his dedication in guiding me throughout my journey over the last two years. I certainly wouldn't have completed this work without your ceaseless support. I also wish to extend my thanks to the other group members, past and present, who have made this experience most memorable. Thank you to James, Nazanin, Tareq, Rojan, Dilip, Francesco and everybody else for the fun and enlightening conversations we have had. I've learned much about parts of the world I wouldn't have otherwise given much thought, and I wish to thank you for that, but most of all, I want to thank you each and every one for letting me share my life with you. I love this group. I would like to thank my family, especially my mom, for the encouragement during my successes and comfort during my difficulties. Thanks to my Auntie Christie for hyping me up to the rest of my family. I want to thank my boyfriend, RJ, who has been in my life for only a little while, but he has brightened up each and every day. I love you.

Lastly, in memory of Roger C. Howard, who did not live long enough to see the man I would become. I love you, and I miss you.

Author Contributions

The research presented in this thesis constitutes original scientific work.

For the first project, which investigated the evolution of spatial correlations in SPDC beyond the standard thin-crystal approximation, the original concept was developed by Alessio D'Errico and Ebrahim Karimi. The theoretical framework was established by Roohollah Ghobadi, Alessio D'Errico, and Christian Howard. Numerical simulations were carried out by Christian Howard under the guidance of Alessio D'Errico. The experimental work was designed by Nazanin Dehghan and performed by Alessio D'Errico, with contributions from Roohollah Ghobadi and Christian Howard. The project was supervised by Ebrahim Karimi.

The second project focused on the evolution of spatially correlated photon pairs under tight-focusing conditions. The research direction was conceived by Alessio D'Errico and Ebrahim Karimi. The theoretical analysis and mathematical derivations were performed by Christian Howard. The project was supervised by Ebrahim Karimi.

Contents

List of Figures

1

Introduction

In 1873, James Clerk Maxwell published his work, "A Treatise on Electricity and Magnetism", which unified our understanding of electricity and magnetism into a single theoretical framework now known as Classical Electrodynamics. From then until the onset of the 20th century, Maxwell's Electromagnetic Theory, along with Newton's Mechanics, was thought to describe all of physical reality. However, in the early 20th century, problems such as the ultraviolet catastrophe, the photoelectric effect, and the need to explain the gross structure of atoms led to the discovery of a new type of physics we call Quantum Mechanics, which showed that energy comes in indivisible chunks called quanta [1, 2, 3]. This was spectacularly successful in explaining the structure of atoms and in predicting the discrete frequencies at which atoms and molecules absorb and emit light. One of the most fortuitous concepts of quantum theory is that of the photon, which was coined by Albert Einstein in his 1905 account of the photoelectric effect [2], although it had previously been indirectly considered by Max Planck. Today, our understanding of the photon and light-matter interactions has matured significantly since the early 20th century and is foundational to the development of some of the most important technologies of our time, such as the laser. Our modern understanding of what a photon is only vaguely resembles Einstein's conception. Today, photons are widely used in quantum optics, information theory, and quantum computing. Of great importance is entanglement - an intrinsically quantum mechanical phenomenon. For a composite system to be entangled with respect to some system property, the measurements made on one subsystem cannot be made independently of the measurements performed on the other subsystem. Back in 1935, Albert Einstein, along with Boris Podolski and Nathan Rosen, invoked an entanglement-based argument to claim that quantum mechanics was an incomplete theory [4]. This famous work, known as the EPR paradox, sparked extensive discussion about the compatibility of local-realistic hidden-variable models with quantum mechanics. Today, entanglement is no longer relegated to mere thought experiments or fundamental tests of quantum theory; it has found abundant applications in information processing, communications, computing, cryptography, and imaging over the last 30 years. In this chapter, we will develop the relevant concepts from electromagnetic theory and quantum mechanics that we will need in order to understand the research that has been performed for this thesis. This thesis is about the propagation of biphoton pairs produced via Spontaneous Parametric Downconversion (SPDC), the evolution of near-field spatial correlations, and the tight focusing of biphoton pairs with Orbital Angular Momentum (OAM).

1.1 Electromagnetism in Dielectric Media

The behavior of electromagnetic fields is governed by Maxwell's equations, a set of four coupled partial differential equations that relate the electric field $\mathbf{E}$ and magnetic field $\mathbf{B}$ to their sources, namely charge ρ and current $\mathbf{J}$ distributions. Together with appropriate boundary conditions, these equations provide a complete description of the generation, propagation, and interaction of electromagnetic fields in both free space and materials. For a dielectric medium characterized by permittivity ϵ, permeability μ, charge density ρ, and current density $\mathbf{J}$, Maxwell's equations can be written as [5]

$$\nabla \cdot \mathbf{D} = \rho \tag{1.1}$$

$$\nabla \cdot \mathbf{B} = 0 \tag{1.2}$$

$$\boldsymbol{\nabla} \times \mathbf{E} = -\frac{\partial \mathbf{B}}{\partial t} \tag{1.3}$$

$$\boldsymbol{\nabla} \times \mathbf{H} = \mathbf{J} + \frac{\partial \mathbf{D}}{\partial t}. \tag{1.4}$$

Maxwell's equations in matter are accompanied by constitutive relations $\mathbf{D} = \epsilon \mathbf{E} = \epsilon_0 \mathbf{E} + \mathbf{P}$ and $\mathbf{B} = \mu \mathbf{H} = \mu_0(\mathbf{H} + \mathbf{M})$, where $\mathbf{P}$, and $\mathbf{M}$ are the material electric and magnetic polarizations, respectively. In a linear, homogeneous and isotropic dielectric in which there are no free charges and currents, we can easily show that the electric and magnetic fields solve the linear wave equation

$$\nabla^2 \mathbf{E} - \frac{1}{c^2}\frac{\partial^2 \mathbf{E}}{\partial t^2} = \mu_0 \frac{\partial^2 \mathbf{P}}{\partial t^2} \tag{1.5}$$

$$\nabla^2 \mathbf{B} - \frac{1}{v^2}\frac{\partial^2 \mathbf{B}}{\partial t^2} = 0, \tag{1.6}$$

where $c = \frac{1}{\sqrt{\epsilon_0 \mu_0}}$, and $v = \frac{1}{\sqrt{\epsilon \mu}}$, are the speed of electromagnetic waves in vacuum and inside a material with permittivity of ϵ, and permeability of μ respectively. Many dielectric materials, including those studied in this thesis, are not magnetic therefore the magnetic permeability is equal to the permeability of free space hence $\mu = \mu_0$. These two vector wave equations describe the propagation of transverse electromagnetic waves – recall that $\mathbf{E}$ and $\mathbf{B}$ are divergence-free. In practice, we need not solve both wave equations; we may only solve the electric field $\mathbf{E}$ and then integrate equation (1.3) to obtain the magnetic field. We see that in dielectric matter, the second time derivative of the polarization takes the place of a source term driving electromagnetic waves in the material.

The polarization term can be written as the sum of a linear and non-linear term, such as $\mathbf{P} = \mathbf{P}^L + \mathbf{P}^{NL}$. In anisotropic materials such as most crystals, the linear polarization term is expressed in Einstein summation notation as $P_i^L = \epsilon_0 \chi_{ij}^{(1)} E_j$ where $\chi_{ij}^{(1)}$ is a rank-2 tensor called the *dielectric susceptibility tensor*. This implies that the direction of material polarization is in general not collinear with the electric field. The material response in linear polarization is essentially that of a coherently driven harmonic oscillator generating light at the driving frequency. The end result is that light propagating in a linear material preserves its frequency but propagates through the material at a slower speed than light in vacuum. When the material is homogeneous and isotropic, the susceptibility tensor becomes a scalar quantity. The non-linear polarization term $\mathbf{P}^{NL}$ is responsible for the generation of new optical frequencies. The non-linear polarization term is acquired when decomposing the electric polarization into a power series and collect together the higher order terms. Therefore the non-linear polarization term, $\mathbf{P}^{NL}$, is written in Einstein summation notation in the following form,

$$\mathbf{P}_i^{NL} = \epsilon_0 \chi_{ijk}^{(2)} E_j E_k + \epsilon_0 \chi_{ijkl}^{(3)} E_j E_k E_l + ... \tag{1.7}$$

Here $\chi_{ijk}^{(2)}$ is the second order non-linear susceptibility tensor which is a third-rank tensor and similarly $\chi_{ijkl}^{(3)}$ is a fourth-rank tensor representing the third-order non-linear susceptibility. The expansion continues into higher order terms following the same pattern. Second order non-linear optical processes are the concern of this thesis, and governs well understood optical phenomena such as sum frequency generation and parametric down-conversion [6]. Non-linear polarization in ordinary circumstances is negligible since non-linear polarization responses require strong fields that can only be produced from powerful lasers in order to be observed.

The linear wave equation has been extensively studied, and in optics, it is standard to suppose a solution of the form $\mathbf{E}(\mathbf{r}, t) = \mathbf{E}(\mathbf{r})e^{-i\omega t}$ where $\mathbf{E}(\mathbf{r})$ is some complex field amplitude. It should be noted that the use of a complex representation of the electric field is only a convenient mathematical abstraction. An electric field is a physical quantity, therefore it is a real-valued vector function. Thus, the physical field itself is obtained by adding the complex conjugate to $\mathbf{E}(\mathbf{r}, t)$ and dividing the expression by 2, or by simply keeping in ones mind that when the computations are over we take the real part of the electric field as this is the physically meaningful quantity. Substituting this into (1.5), we arrive at the *Helmholtz equation*

$$\nabla^2\mathbf{E}(\mathbf{r}) + k^2\mathbf{E}(\mathbf{r}) = 0, \tag{1.8}$$

where $k = n\omega/c$ is the wavevector. The Helmholtz equation can be solved by taking a transverse Fourier transform and solving the simplified equation for the longitudinal coordinate z. Carrying out this simple procedure, we arrive at the *angular spectrum representation* of the field,

$$\mathbf{E}(x, y, z) = \iint_{-\infty}^{\infty} dk_x\, dk_y\, \tilde{\mathbf{E}}(k_x, k_y, 0)\, e^{\pm i\left(\sqrt{k^2 - k_x^2 - k_y^2}\right)z}. \tag{1.9}$$

Here, $\tilde{\mathbf{E}}(k_x, k_y, 0)$ is the pupil field. The Helmholtz equation is an elliptic partial differential equation whose solutions have also been extensively studied. In optics, we typically generate waves that propagate in a specific direction, say, the positive z direction, and with a small divergence angle, such as laser beams. These fields can be given the following tentative solution $\mathbf{E}(\mathbf{r}) = \mathbf{A}(\mathbf{r})\, e^{ikz}$. When substituted back into (1.8), we get,

$$\frac{\partial^2\mathbf{A}}{\partial x^2} + \frac{\partial^2\mathbf{A}}{\partial y^2} + 2ik\frac{\partial\mathbf{A}}{\partial z} + \frac{\partial^2\mathbf{A}}{\partial z^2} = 0.$$

Now we invoke the *slowly varying envelope approximation* (SVEA), which means that on the order of approximately a wavelength $|\frac{\partial\mathbf{A}}{\partial z}|$ is really small, and that means $|\frac{\partial^2\mathbf{A}}{\partial z^2}|$ is even smaller, and we can just forget about it altogether. Our final result is called the *paraxial wave equation*,

$$\frac{\partial^2\mathbf{A}}{\partial x^2} + \frac{\partial^2\mathbf{A}}{\partial y^2} + 2ik\frac{\partial\mathbf{A}}{\partial z} = 0. \tag{1.10}$$

There are several famous families of solutions to the paraxial wave equation. Hermite-Gaussian (HG) and Laguerre-Gaussian (LG) beams are two classes of solutions in Cartesian and cylindrical coordinates, respectively. These are solutions to (1.10) that maintain a constant transverse profile, apart from scaling, in the beam as the beam propagates. Each set of solutions is obtainable by solving (1.10) by separation of variables in various coordinate systems. The Hermite-Gaussian beam is obtained through separable solutions in Cartesian coordinates, the fundamental solution of which corresponds to the Gaussian beam. The family of Hermite-Gauss beams is given by

$$\begin{aligned} \mathbf{E}_{n,m}(x,y,z) =& E_{n,m}\frac{W_0}{W(z)}G_n\left(\frac{\sqrt{2}x}{W(z)}\right)G_m\left(\frac{\sqrt{2}y}{W(z)}\right) \\ &\times \exp\left(-ikz - ik\frac{(x^2+y^2)}{2R(z)} + i(n+m+1)\zeta(z)\right), \end{aligned} \tag{1.11}$$

where $G_n(u) = H_n(u)e^{\frac{u^2}{2}}$ and $H_n(u)$ is the n^{th} Hermite polynomial and $E_{n,m}$ are coefficients chosen so that the beam is properly normalized. We have other beam parameters such as $W(z)$, which is the transverse beam width at some distance z, $R(z)$ is the wavefront radius of curvature and $\zeta(z)$ is the Guoy phase, which represents the extra phase the beam accumulates upon propagation as a result of the change in the wavefront radius of curvature. These parameters have the following forms,

$$W_0 = \frac{\lambda z_0}{\pi} \tag{1.12}$$

$$W(z) = W_0\sqrt{1+\frac{z^2}{z_0^2}} \tag{1.13}$$

$$R(z) = z\left(1+\frac{z^2}{z_0^2}\right) \tag{1.14}$$

$$\zeta(z) = \arctan\left(\frac{z}{z_0}\right). \tag{1.15}$$

The fundamental mode of the HG beam is found by setting $n = m = 0$, which yields the famous Gaussian beam solution

$$\mathbf{E}_{0,0}(x,y,z) = E_{0,0}\left[\frac{W_0}{W(z)}\right]\exp\left\{\frac{-(x^2+y^2)}{W(z)^2}\right\}\exp\left\{-ikz - ik\frac{(x^2+y^2)}{2R(z)} + i\zeta(z)\right\}. \quad (1.16)$$

The Gaussian beam has a circular intensity cross-section, making it ideal for industrial uses such as laser materials processing [7]. Another famous set of solutions can be found by separating variables in cylindrical coordinates (ρ, θ, ϕ),

$$\begin{aligned}\mathbf{E}_{\ell,p}(\rho,\phi,z) = E_{\ell,p}\left(\frac{W_0}{W(z)}\right)\left(\frac{\rho}{W(z)}\right)^{|\ell|} L_p^\ell\left(\frac{2\rho^2}{W^2(z)}\right) e^{\frac{-\rho^2}{W^2(z)}} \\ \times \exp\left(-ikz - ik\frac{\rho^2}{2R(z)} + i\ell\phi + i(2p + |l|+1)\zeta(z)\right),\end{aligned} \quad (1.17)$$

where p and ℓ are radial and azimuthal indices that are positive integers and integer numbers, respectively. The Laguerre-Gauss beams are particularly important since they carry orbital angular momentum (OAM) with topological charge ℓ (each photon carries OAM of $\hbar\ell$ along propagation direction). LG beams are typically produced in the lab by phase encoding and intensity masking [8] as well as exciting different modes in a laser cavity [9]. There has been a great deal of interest in the OAM of the LG beams, and they have found applications in micromachining, optical trapping, communications and metrology [10, 11]. In addition to carrying OAM, Laguerre-Gaussian modes exhibit radial phase discontinuities characterized by the radial index p, giving rise to $p + 1$ intensity maxima in the transverse plane.

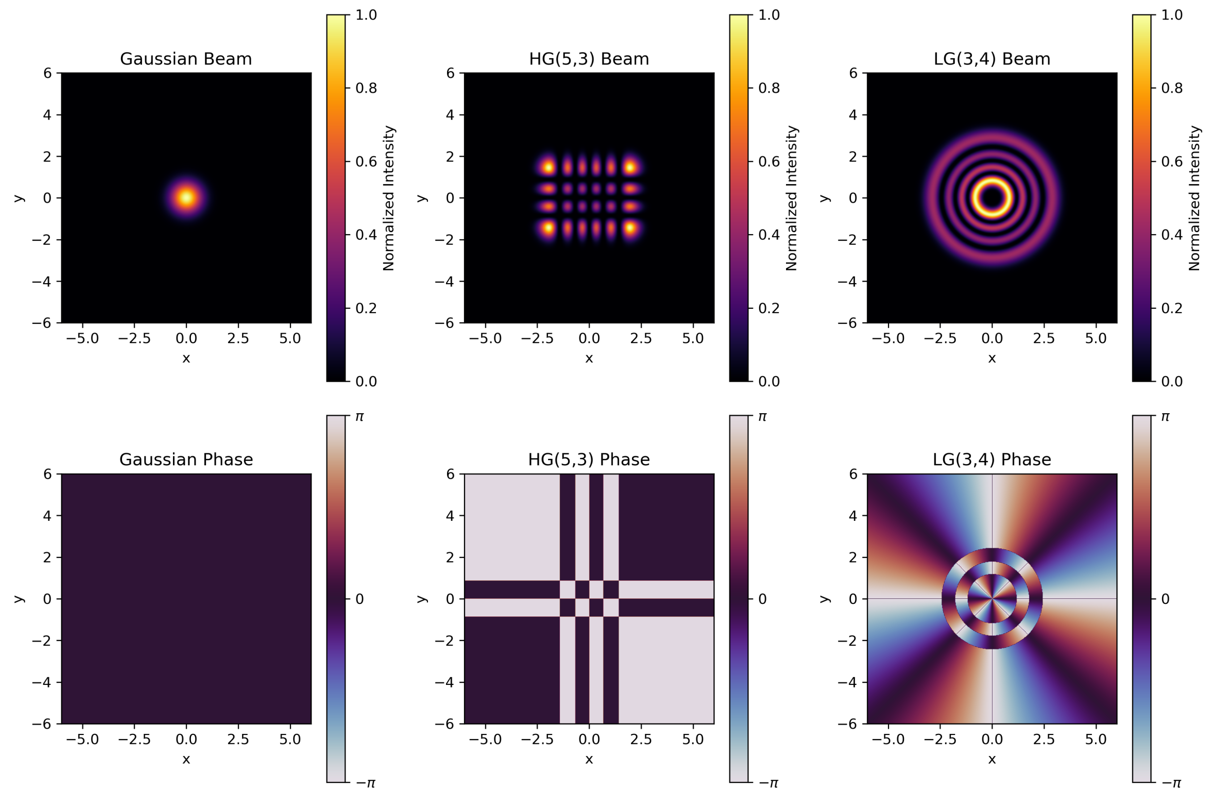

Figure 1.1: Transverse intensity and phase profiles obtained from numerical simulations for a Gaussian beam, an $\mathrm{HG}_{5,3}(x, y)$ mode, and an $\mathrm{LG}_{3,4}(\rho, \phi)$ mode. Intensities are normalized to their peak values, whereas phases are encoded using a hue color map covering the interval $[-\pi, \pi]$.

1.2 Vector Vortex Beams and Orbital Angular Momentum

An important class of optical beams are Vector Vortex Beams (VVB). These are beams whose transverse cross-sections contains points where the phase is undefined. These points are called *phase singularities*. In the neighborhood of a phase singularity the phase changes as an integer multiple of 2π. Hence along a closed curve containing the phase singularity the phase changes as $2\pi\ell$ where ℓ is the *topological charge* of the singularity. The theory of vortices in optical fields was pioneered by Nye and Berry in their seminal 1974 work [12]. However, it wasn't until 1992 that a method was discovered to convert higher-order Hermite-Gauss modes into Laguerre-Gauss modes with the use of two cylindrical lenses by introducing Guoy phase shifts along the horizontal and vertical directions [13]. Today there are many ways that vortex beams are generated in the lab, including but not limited to spiral phase plates, q-plates, spatial light modulators, computer generated holograms along with phase and intensity masking techniques [8, 14, 15]. Vortex beams have helical phase-fronts as they propagate, induced by mathematical terms of the sorts $e^{i\ell\phi}$, and this structure gives rise to a wave-vector that has an azimuthal component. This induces a helical transport of energy as the beam propagates, as opposed to the rectilinear propagation of electromagnetic energy in a plane wave. This transport of energy is directly associated with the *orbital angular momentum* of the beam [16, 17]. This is to be distinguished from the transport of spin angular momentum by circularly polarized light, which arises from the intrinsic spin of a photon, the OAM arises from the spatial structure of the optical field itself. Vector vortex beams not only transport OAM but acquire intricate three-dimensional polarization structures and topologies such as a Möbius strip [18]. It is for these reasons that vector beams transporting OAM have generated significant interest in their application to structured light and have been at the center of major technological advancements in recent decades. The ability of OAM beams to transfer angular momentum to matter has also made them an important tool in optical manipulation of microscopic and nanoscopic particles. When particles interact with an OAM beam, orbital angular momentum is transferred from the optical field to the particle producing a controllable torque. This has been widely exploited in optical tweezers where OAM beams can trap and induce a controlled rotation in a microparticle driving the development of micromachines [19]. OAM beams have also generated significant interest in information and communications science. This is due to the fact that a large number of orthogonal OAM modes enable the implementation of high-dimensional encoding schemes capable of increasing information capacity in both classical and quantum information protocols for free space optical communications [20]. Moreover, OAM beams have been massively influential in fiber optics communications where mode division multiplexing techniques have allowed for high-capacity transmission of optical information [21].

In microscopy OAM beams have been transformative in allowing scientists to investigate materials at scales on the order of a wavelength. Super-resolution with OAM beams is achieved in stimulated emission depletion microscopy (STED), which uses the ring-shaped intensity profile of a Laguerre-Gauss beam to suppress fluorescence. This selective suppression of fluorescence allows for imaging at resolutions beyond the diffraction limit and even single molecule localization [22]. Beyond STED microscopy, OAM beams have found applications in phase-contrast and structured illumination microscopy [14]. Other commonly used types of vector vortex beam are the radially and azimuthally polarized “donut” modes which can be focused beyond the limits imposed by scalar diffraction and produce strong longitudinal fields in the focal region. The unique polarization structures in vector vortex beams gives them complex focusing properties such as mode-mixing, and when quantum effects are important, spin-orbit coupling. These properties have made structured light imperative in nano-scale imaging, plasmonics, and near-field microscopy where enhanced spatial resolution and precisely controlled light-matter interactions are essential.

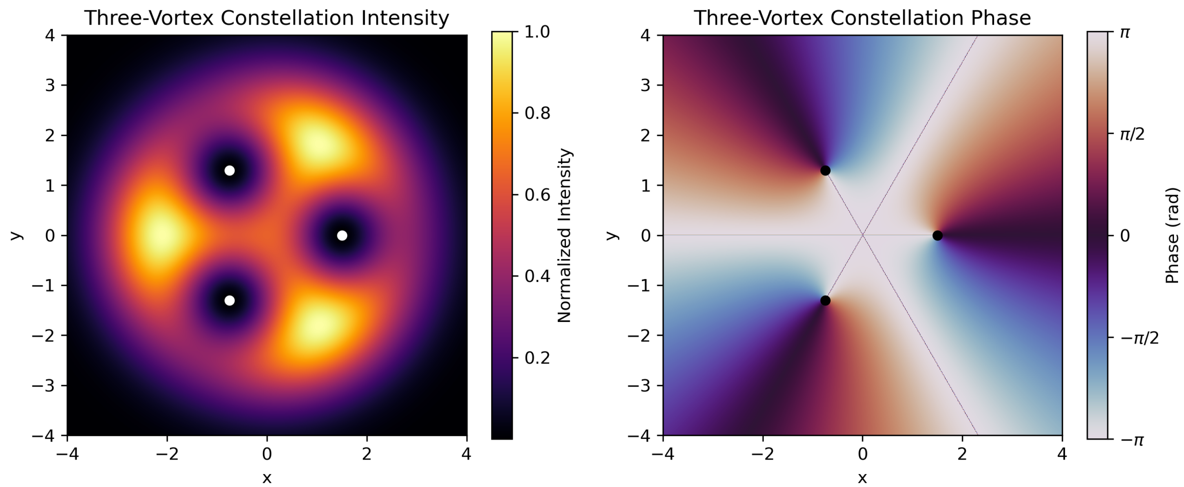

Figure 1.2: Three optical vortices in a triangular distribution along with the phase distribution. The plot is generated with the state $E(x,y) = e^{-(x^2+y^2)/4}\prod_{n=1}^{3}((x-x_n)+i(y-y_n))$. Where $(x_n, y_n) = (r_0\cos(\frac{2\pi n}{3}), r_0\sin(\frac{2\pi n}{3}))$, with $r_0 = 1.5$.

1.3 Introductory Quantum Theory

1.3.1 Historical Background

Quantum mechanics describes the behavior of microscopic particles that compose material systems. Its success in describing our microscopic world, and the second technological revolution that it has ushered in, surely makes quantum theory the crowning intellectual achievement of the 20$^{\text{th}}$ century - if not of all time. Quantum mechanics is rather (in)famous for the plethora of counter-intuitive predictions that have puzzled many a student and scientist alike. This understanding of the world was arrived at, not because anybody would have really imagined that this is the way the world *ought* to be, but because they were forced to by experimental observations. Common retellings of the history of quantum mechanics begin with the story of Max Planck's resolution of the blackbody problem in 1900. For a perfectly absorbing body, classical electromagnetic theory predicts that the total energy radiated by the body when integrated over all frequencies is infinite, which is impossible. Max Planck solved the problem by imagining that the body was composed of many identical oscillators that can only exist in a discrete set of energies, and he derived the famous Planck spectrum [1]. Then, in 1905, Albert Einstein was working at a Swiss patent office when he began to write his musings on why different metals emit electrons at different minimum frequencies - the photoelectric effect. In this work, Einstein drew inspiration from Planck and introduced the concept of the photon; however, the term "photon" was not introduced until later. Einstein imagined light waves as composed of indivisible corpuscles of energy, where the energy of each photon is determined by its frequency and given by $E = h\nu$, where h is Planck's constant and ν is the frequency. His successful account of the photoelectric effect by his photon hypothesis secured him the 1921 Nobel prize. In that same year, Einstein also performed work on the theory of Brownian motion. He provided a method for computing Avogadro's number and thus paved the way to compute the masses of atoms and molecules, thereby eradicating any remaining doubt about their existence in the physics community [23]. In 1913, Niels Bohr proposed a model of the atom based on the previous work of Ernest Rutherford, in which he described atoms as composed of a positively charged nucleus with electrons in classical orbits, which are permitted to "jump" between orbits by the absorption or emission of a photon. Bohr's model successfully predicted the gross structure of the hydrogen atom [3]. Then, in 1924, Louis de Broglie was inspired by Einstein's work and hypothesized that material particles such as electrons could also behave as waves [24]. The existence of matter waves was confirmed by the Davisson-Germer experiments, which showed that electrons undergo diffraction when scattered off a nickel crystal. In 1925, Werner Heisenberg - in collaboration with Max Born and Pascual Jordan - established the matrix mechanics formalism of quantum mechanics; however, it was met with much controversy at the time. The following year, in 1926, Erwin Schrödinger established the wave mechanics formalism and introduced the Schrödinger equation [25], which governs the time evolution of quantum mechanical systems.

1.3.2 Hilbert Space and Quantum States

In quantum mechanics, the principal mathematical objects of study are Hilbert spaces and the linear transformations defined on them. What is a Hilbert space? A Hilbert space is a vector space equipped with an inner product such that the metric induced by the inner product makes our vector space into a complete metric space, which essentially means we can do calculus on it. We identify elements of a Hilbert space using Dirac's Bra-Ket notation; therefore, a vector in Hilbert space is written as a "ket" like $|\psi\rangle \in H$. All finite-dimensional inner-product spaces are Hilbert spaces [26]. Infinite-dimensional spaces are not necessarily Hilbert spaces. An import class of Hilbert spaces are called *separable*, meaning that the space has an orthonormal set of vectors, S, where the span of S is dense in H - implying that a vector in H is either in the span of S or is at worst the limit of a sequence of vectors in the span of S [27]. This is the best we can do to equip an infinite-dimensional space with a basis. In quantum mechanics, dynamical variables such as position and momentum are represented by linear operators in Hilbert space. This is a significant mathematical departure from classical mechanics, where observables are real functions parametrized with respect to time. Since experimental measurements return real values, the operators representing observables in quantum mechanics are self-adjoint, where the operator eigenvalues correspond to the possible results of a measurement, and their eigenvectors correspond to the resulting state the system is found in. Also, operators in Hilbert space in general do not commute with one another. This gives rise to another uniquely quantum feature, observable incompatibility. This refers to the inability to simultaneously specify two observables precisely. An important space of operators is the space of trace-class operators from the Hilbert space into itself, which we will call $T(H)$. A trace-class operator is an operator upon which the trace can be defined. Not all operators in a separable Hilbert space are trace-class, since the series they generate may not converge. This technicality does not arise in finite dimensions, hence all operators are trace-class in a finite-dimensional Hilbert space. Moreover, trace-class operators possess the desirable property that they are *compact* operators, and therefore permit the Singular

Value Decomposition and Schmidt Decomposition, the latter of which is frequently used to examine entanglement in bipartite systems [28, 29].

We identify a quantum state on a Hilbert space (H) with a positive operator of unit trace. Hence, the state space for a quantum system is

$$S(H) := \{\hat{\rho} \in T(H) | Tr(\hat{\rho}) = 1 \quad \text{and} \quad \langle\psi| \hat{\rho} |\psi\rangle \geq 0 \quad \text{for all} \quad \psi \in H\},$$

where, $Tr(.)$ stands for the trace.

The *density operators*, $\hat{\rho}$, are used to describe two kinds of quantum state: *pure* states and *mixed* states. Pure states are identified with projection operators written in the form $\hat{\rho} = |\phi\rangle \langle\phi|$ where $|\phi\rangle \in H$ is a unit vector. Geometrically speaking, the pure states correspond to the *extremal points* of the state space $S(H)$. Pure states contain the maximal amount of information for a given system [28, 30]. Mixed states, on the other hand, are a statistical mixture of projection operators which may be written as $\hat{\rho} = \sum_j p_j |\psi_j\rangle \langle\psi_j|$ where the p_j represents the probability of the system being in state $|\psi_j\rangle$. Mixed states may not possess complete information about a system since not every density operator corresponds to a projection onto some unit vectors. In order to quantify how mixed or pure a state is, we have the *purity* which is calculated by taking $\text{Purity}(\hat{\rho}) := Tr(\hat{\rho}^2)$ [31]. For a density operator representing a quantum state in a Hilbert space of dimension $d < \infty$, we have the following inequality

$$\frac{1}{d} \leq Tr(\hat{\rho}^2) \leq 1,$$

where a purity of 1 implies that the density operator is in a pure state and a purity of $1/d$ means that the state is *maximally mixed* [32]. It is interesting to note as well that any mixed state on some Hilbert space can be expressed as a pure state in a larger Hilbert space [31]. Mixed states can be generated by a preparation of a quantum state into a pure state that is randomly selected from some ensemble of projection operators. They can also be generated from pure states of a composite system by averaging over the results of the other system component [28]. It is interesting to note that given some density operator, $\hat{\rho}$, the decomposition into a sum of projection operators is not unique. In fact, there are infinitely many decompositions available to some given density operator.

1.3.3 Bipartite Systems and Entanglement

Suppose we have a quantum system composed of subsystems A and B. The Hilbert spaces for the subsystems are denoted by H_A, H_B and the total Hilbert space for the composite system is constructed by taking the tensor product $H = H_A \otimes H_B$. A quantum state $|\Psi\rangle \in H$ is called *separable* if it can be written in the form $|\Psi\rangle = |\psi_A\rangle \otimes |\psi_B\rangle$ for some pair of vectors $|\psi_A\rangle \in H_A$ and $|\psi_B\rangle \in H_B$. Otherwise, it is called *entangled*. It is not difficult to come up with examples of entangled pure states, such as the spin states of entangled electrons

$$\frac{1}{\sqrt{2}}(|\uparrow,\downarrow\rangle - |\downarrow,\uparrow\rangle) \in \mathbb{C}^2 \otimes \mathbb{C}^2,$$

where $|\uparrow\rangle$ and $|\downarrow\rangle$ represent the electron's spin up and down states, respectively.

For a quantum state to become entangled with respect to some degree of freedom, we mean that the measurements of system A cannot be made independently of those on system B. As mentioned at the start of this thesis, the EPR paper in 1935 attempted to use entanglement to argue that quantum mechanics was an incomplete theory, which led to extensive research into local hidden-variable models [4]. In 1964, John Bell derived statistical inequalities comparing hidden-variable models with quantum mechanics, known as the *Bell inequalities* [33]. The violation of Bell's inequalities shows that quantum theory, as we know it, holds and cannot be described by local hidden variables. However, today, entanglement isn't just relegated to fundamental tests of quantum theory; it's also extensively exploited as a resource in quantum information processing, imaging, and communications. For example, the quantum superdense coding protocol uses maximally entangled pairs to transmit two classical bits of information in a single use of a quantum channel. An important mathematical question is the identification of entanglement for a given pure state in a bipartite system. The most common way of answering this is with the *Schmidt decomposition*, where any vector having Schmidt rank greater than 1 is entangled.

To determine whether a mixed state is entangled is a much more subtle problem. For pure states given by a projection operator $\hat{\rho}_{AB} = |\psi_{AB}\rangle \langle\psi_{AB}|$ the density operator is trivially separable whenever $|\psi_{AB}\rangle$ is separable. For a general bipartite density operator $\hat{\rho}_{AB}$, the state is separable if and only if it can be written as a convex combination of tensor products of density operators on H_A and H_B. In other words a density operator is separable if there exists $\{\hat{\rho}_A\}_{i=1}^k \subset S(H_A)$ and $\{\hat{\rho}_B\}_{i=1}^k \subset S(H_B)$ so that the bipartite state $\hat{\rho}_{AB}$ can be written as [29],

$$\hat{\rho}_{AB} = \sum_{i=1}^{k} p_i \left(\hat{\rho}_{A_i} \otimes \hat{\rho}_{B_i}\right).$$

1.3.4 The Quantum Harmonic Oscillator

The quantum harmonic oscillator is probably the most important system in all of quantum mechanics, and it is worth reviewing this system as it leads us to the quantization of the electromagnetic field. We follow the treatment as presented in [34]. Consider the following single-particle Hamiltonian

$$\hat{H} = \frac{\hat{p}^2}{2m} + \frac{m\omega^2\hat{x}^2}{2}, \tag{1.18}$$

and recall the canonical commutation relation $[\hat{x}, \hat{p}] = i\hbar$. Here, m is the mass of the particle, ω is the oscillation frequency of the harmonic oscillator, and x and p are the particle position and momentum, respectively. We can then build the *ladder operators* along with their commutator,

$$\hat{a} = \sqrt{\frac{m\omega}{2\hbar}}(\hat{x} + i\frac{\hat{p}}{m\omega}), \quad \hat{a}^\dagger = \sqrt{\frac{m\omega}{2\hbar}}(\hat{x} - i\frac{\hat{p}}{m\omega}), \quad [\hat{a}, \hat{a}^\dagger] = 1. \tag{1.19}$$

Then the Hamiltonian can be written as,

$$\hat{H} = \hbar\omega(\hat{a}^\dagger\hat{a} + \frac{1}{2}). \tag{1.20}$$

Define the *number operator*, $\hat{N} = \hat{a}^\dagger\hat{a}$. The eigenstates of the Hamiltonian are the eigenstates of the number operator. The number operator is self-adjoint, so there exist orthonormal eigenvectors with real eigenvalues [26]. We will write these eigenvectors as $|n\rangle$, where $\hat{N}|n\rangle = n|n\rangle$. The number operator does not commute with the raising and lowering operators,

$$[\hat{N}, \hat{a}] = -\hat{a}, \quad [\hat{N}, \hat{a}^\dagger] = \hat{a}^\dagger. \tag{1.21}$$

We now easily see that the eigenvalues of the Hamiltonian are $E_n = \hbar\omega(n + \frac{1}{2}), n \in \mathbb{Z}^+$. Using (1.20), we can easily see that the effect of $\hat{a}$ and $\hat{a}^\dagger$ is to decrease or increase the eigenvalue of the number operator by one,

$$\hat{N}\hat{a}|n\rangle = (n-1)\hat{a}|n\rangle, \quad \hat{N}\hat{a}^\dagger|n\rangle = (n+1)\hat{a}^\dagger|n\rangle,$$

hence the term ladder operators. Relations (13-15) are sufficient to solve the problem entirely, and this representation is referred to as the *number state representation*. To determine the corresponding wavefunctions substitute $y = \sqrt{\frac{m\omega}{\hbar}}x$ to transform the ladder operators to

$$\hat{a}^\dagger = \frac{1}{\sqrt{2}}(y - \frac{\mathrm{d}}{\mathrm{d}y}), \quad \text{and} \quad \hat{a} = \frac{1}{\sqrt{2}}(y + \frac{\mathrm{d}}{\mathrm{d}y}).$$

Applying the lowering operator to the ground state, we have,

$$0 = \hat{a}\psi_0(y) = \frac{1}{\sqrt{2}}(y - \frac{\mathrm{d}}{\mathrm{d}y})\psi_0(y) \implies \psi_0(y) = C_0 e^{-y^2/2}. \tag{1.22}$$

where C_0 is the normalization constant. Then we generate the n^{th} state by applying the raising operator, $\hat{a}^\dagger$, to the ground state wavefunction n-times. Observing that the raising operator is just the Rodrigues formula for the Hermite Polynomials and knowing the following orthogonality relation,

$$\int H_m(y)H_n(y)e^{-y^2/2}dy = \sqrt{\pi}2^n n!\,\delta_{m,n}.$$

We now arrive at the normalized wavefunctions,

$$\psi_n(y) = \sqrt{\frac{1}{\sqrt{\pi}2^n n!}}H_n(y)e^{-y^2/2}, \quad y = \sqrt{\frac{m\omega}{\hbar}}x. \tag{1.23}$$

1.3.5 The Quantization of the Electromagnetic Field

Now that we've discussed the quantum harmonic oscillator, we can move on to the quantization of free radiation. For this section, we will suppose we are in free space with no free currents or charges, and our analysis follows the treatments as presented in [30, 35]. The electric and magnetic fields expressed in Maxwell's equations can be written in terms of scalar and vector potentials, which we will write as ϕ and $\mathbf{A}$, respectively. The magnetic field can be expressed in terms of a vector potential, $\mathbf{A}$, as $\mathbf{B} = \boldsymbol{\nabla} \times \mathbf{A}$. The electric field can be expressed in terms of the scalar and vector potential as $\mathbf{E} = -\nabla\phi - \frac{\partial \mathbf{A}}{\partial t}$. If we choose the Coulomb gauge by enforcing $\nabla \cdot \mathbf{A} = 0$, and substituting our $\mathbf{E}$ and substituting these relations into Maxwell's equations, we get,

$$\nabla^2\mathbf{A} - \frac{1}{c^2}\frac{\partial^2 \mathbf{A}}{\partial t^2} = 0 \tag{1.24}$$

$$\nabla^2\phi = 0. \tag{1.25}$$

To quantize the electromagnetic field, it is useful to consider a quantization cavity. So we imagine a large rectangular cavity with side length L that is much larger than the wavelengths contained within it. We solve (1.24) by supposing that $\mathbf{A}$ has time harmonic solutions and demand that the spatial distribution satisfy periodic boundary conditions.

The corresponding solutions are plane-wave solutions of the form

$$\mathbf{A} = \sum_{\mathbf{k},s} \mathbf{e}_{\mathbf{k},s}[\mathbf{A}_0 e^{i(\mathbf{k}\cdot\mathbf{r}-\omega t)} + \mathbf{A}_0^* e^{-i(\mathbf{k}\cdot\mathbf{r}-\omega t)}], \quad \mathbf{k} = \frac{2\pi}{L}(n_x, n_y, n_z), \tag{1.26}$$

where the sum is over all wave-vectors and polarization. We now compute the total energy in the fields over the volume V,

$$H = \frac{1}{2}\int_V \left(\epsilon_0|\mathbf{E}|^2 + \frac{1}{\mu_0}|\mathbf{B}|^2\right) dV = 2\epsilon_0 V \sum_{\mathbf{k},s} \omega_k^2 \mathbf{A}_{\mathbf{k},s}\mathbf{A}_{\mathbf{k},s}^*. \tag{1.27}$$

Where the latter portion of this final equation closely resembles the harmonic oscillator Hamiltonian in the number state representation, where our coefficients $\mathbf{A_0}$ and $\mathbf{A_0}^*$ take the place of the raising and lowering operators. Along that train of thought, we arrive at the quantized field expressions by,

$$\mathbf{A}_{\mathbf{k},s} = \frac{1}{2\omega_k\sqrt{\epsilon_0 V}}(\omega_k \mathbf{x}_{\mathbf{k},s} + i\mathbf{p}_{\mathbf{k},s}), \quad \mathbf{A}_{\mathbf{k},s} = \frac{1}{2\omega_k\sqrt{\epsilon_0 V}}(\omega_k \mathbf{x}_{\mathbf{k},s} + i\mathbf{p}_{\mathbf{k},s}). \tag{1.28}$$

Substituting (1.27) into (1.26) gives,

$$H = \frac{1}{2}\sum_{\mathbf{k},s}(\mathbf{p}_{\mathbf{k},s}^2 + \omega_k^2 \mathbf{x}_{\mathbf{k},s}^2). \tag{1.29}$$

Which we identify as a sum of harmonic oscillator Hamiltonians from the previous section, where the sums take place over all wave-vectors and polarizations. The quantization now occurs by identifying the position and momentum variables with their hermitian operators by $\mathbf{p}_{\mathbf{k},s} \mapsto \hat{\mathbf{p}}_{\mathbf{k},s}$ and $\mathbf{x}_{\mathbf{k},s} \mapsto \hat{\mathbf{x}}_{\mathbf{k},s}$. The position and momentum operators satisfy the canonical commutation relation and therefore the corresponding quantized vector potential satisfies the commutation relations for raising and lowering operators in 1.19. We then arrive at the quantized Hamiltonian for a multi-mode field,

$$\hat{H} = \hbar\omega_k \sum_{\mathbf{k},s} \left(\hat{\mathbf{A}}_{\mathbf{k},s} \hat{\mathbf{A}}^*_{\mathbf{k},s} + \frac{1}{2} \right). \tag{1.30}$$

The quantized electromagnetic field corresponds to a set of harmonic oscillator Hamiltonians, and therefore we identify the quanta of the electromagnetic field, *photons*, with quantum harmonic oscillators. We may lastly make use of Maxwell's equations one final time to arrive at the expressions for the electric and magnetic field operators,

$$\hat{\mathbf{E}} = i \sum_{\mathbf{k},s} \omega_k \mathbf{e}_{\mathbf{k},s} [\hat{\mathbf{A}}_{\mathbf{k},s} e^{i(\mathbf{k}\cdot\mathbf{r}-\omega_k t)} + \hat{\mathbf{A}}^*_{\mathbf{k},s} e^{-i(\mathbf{k}\cdot\mathbf{r}-\omega_k t)}] \tag{1.31}$$

$$\hat{\mathbf{B}} = \frac{i}{c} \sum_{\mathbf{k},s} \omega_k (\mathbf{k} \times \mathbf{e}_{\mathbf{k},s}) \mathbf{e}_{\mathbf{k},s} [\hat{\mathbf{A}}_{\mathbf{k},s} e^{i(\mathbf{k}\cdot\mathbf{r}-\omega_k t)} - \hat{\mathbf{A}}^*_{\mathbf{k},s} e^{-i(\mathbf{k}\cdot\mathbf{r}-\omega_k t)}]. \tag{1.32}$$

Here, $\mathbf{e}_{\mathbf{k},s}$ is the unit vector for each wavevector k, and s is the polarization state which can take two values due to the transversality of the electric and magnetic fields.

1.3.6 The Interaction Picture

In the quantum mechanical formalism, there are three main "pictures" to describe the time evolution of a system. The first is the Schrödinger picture, in which time evolution is incorporated directly into the state vector. Second is the Heisenberg picture, which keeps state vectors fixed in time and instead incorporates time evolution into observables. Lastly, there is the interaction picture, which is a sort of hybrid between the Schrödinger and Heisenberg pictures that is used extensively in the modeling of the interaction of light and matter. Suppose we have a Hamiltonian $\hat{H} = \hat{H}_0 + \hat{H}_I$, where $\hat{H}_0$ is a free Hamiltonian whose solutions are known, and $\hat{H}_I$ is a Hamiltonian describing the interaction between two systems. In the interaction picture, the time evolution of the observables is determined by the free Hamiltonian, and the time evolution of the state vectors is determined by the interaction Hamiltonian in the following way:

$$\hat{H}_I' = e^{i\hat{H}_0 t/\hbar} \hat{H}_I e^{-i\hat{H}_0 t/\hbar} \tag{1.33}$$

$$i\hbar \frac{\partial \left|\psi, t\right\rangle_I}{\partial t} = \hat{H}_I' \left|\psi, t\right\rangle_I , \tag{1.34}$$

we will use the interaction picture in our discussion of the state generated by Spontaneous Parametric Downconversion (SPDC), which is to follow in a later section.

1.3.7 The Winger Function Formalism

In 1932, Eugene Wigner derived the Wigner transform, which is an integral operator from the state space of density matrices into functions on phase space [36]. For a single particle whose state is described by the density operator $\hat{\rho}$, the Wigner function is given by,

$$W(x,p) = \frac{1}{2\pi\hbar} \int_{\infty}^{\infty} \left\langle x + \frac{y}{2} \right| \hat{\rho} \left| x - \frac{y}{2} \right\rangle e^{ipy/\hbar} dy. \tag{1.35}$$

The Wigner function attempts to emulate the phase space probability distribution familiar from classical statistical mechanics. The Wigner function $W(x,p)$ is called a *quasiprobability distribution* since the Wigner function may not necessarily be positive definite. In these circumstances, the Wigner function itself cannot be interpreted as a probability distribution on phase space. The failure of positive definiteness is not a bug but a feature of the Wigner function, for its failure signals to us that we have a non-classical state of light. It is also the case that when the density operator, $\hat{\rho}$, is a pure state, the marginals of the Wigner function do give positive definite distributions that are genuine probability density functions, and therefore the expectation values calculated by the Wigner function correspond to those calculated from the ordinary quantum formalism.

1.3.8 Spontaneous Parametric Down-Conversion

Spontaneous Parametric Down-Conversion (SPDC) is a second-order nonlinear light-matter interaction in which a high-frequency photon is absorbed by a crystal, which then emits two lower-frequency photons while satisfying conservation of energy and momentum. SPDC is vaguely similar to difference frequency generation, but there are important differences. Difference frequency generation is a deterministic process, whereas the down-conversion of SPDC photons is random, and highly inefficient at that; in a Beta-Barium Borate (BBO) crystal only about one in every million photons is down-converted [37]. SPDC is an intrinsically quantum mechanical phenomenon, and it is the primary way that entangled photons are generated in quantum optics laboratories [38]. In our work, we generated SPDC photons in a BBO crystal. A BBO crystal is a negative uniaxial crystal. This means it has one symmetry axis called the optic axis, which has an index of refraction n_o, and an extraordinary axis with an index of refraction n_e. The use of the term *negative uniaxial crystal*, which means that the ordinary index of refraction n_o is greater than the extraordinary index n_e. Satisfying conservation of momentum implies the phase-matching condition, $n_e(2\omega_s) = n_o(\omega_s)$ in type I SPDC. SPDC can only be generated in a non-centrosymmetric crystal, since second-order non-linear phenomena are only possible in crystals lacking a center of symmetry [6]. In the literature, there are two main types of SPDC that are referred to: first, type I, SPDC converts an extraordinary polarized pump photon into two ordinary polarized signal and idler photons ($e \to o + o$), and secondly, type II which converts the extraordinary pump photon into an ordinary and extraordinary signal and idler photon ($e \to e + o$). As previously mentioned, SPDC serves as our primary source of entangled photons, and it has been shown to exhibit entanglement across many different degrees of freedom, depending on the experimenter's intent. We may have polarization entanglement, such as in type-II SPDC, which has been frequently deployed in many Bell test experiments. SPDC photons have shown that spatial entanglement is also desirable to harness for information processing due to the large Hilbert space in continuous variable systems. We may also produce even more exotic types of entanglement depending on the properties of the pump beam, for example, a BBO crystal pumped with an LG beam can produce entanglement in OAM. Entanglement produced through the SPDC process has been shown to be conserved for HG-pumped crystals, along with OAM entanglement in LG-pumped crystals [39, 40]. SPDC has found practical application in quantum key distribution, where entanglement can be exploited in order to securely exchange a cryptographic key between two communicating partners, quantum imaging protocols like ghost imaging, and in quantum computations [41]. This thesis is concerned only with the type I SPDC process. A rough derivation of the two-photon state based on the works of [37, 42, 43] will now be presented. The interaction Hamiltonian for a χ^2 process is

$$\hat{H}_I \propto \int d\mathbf{r} \quad \chi^2 E_p(\mathbf{r},t)\hat{E}_s^+(\mathbf{r},t)\hat{E}_i^+(\mathbf{r},t), \tag{1.36}$$

where we will write out the field operators as sums over k-space as

$$\hat{E}_s^+(\mathbf{r},t) \propto \sum_{\mathbf{k}_s} \hat{a}^\dagger_{\mathbf{k}_s} e^{-i(\mathbf{k}_s\cdot\mathbf{r}-\omega_s t)}$$

and we describe the classical pump beam in the angular spectrum representation

$$E_p(\mathbf{r},t) \propto \int_{-\infty}^{\infty}\int_{-\infty}^{\infty} d\mathbf{k}_{p\perp} d\omega_p \, E_p(\mathbf{k}_{p\perp},\omega_p) e^{i(\mathbf{k}_p\cdot\mathbf{r}-\omega_p t)}.$$

This all gives us the following interaction Hamiltonian

$$\begin{aligned}\hat{H}_I(\mathbf{r},t) = &\int d\mathbf{r} \int_{-\infty}^{\infty} d\mathbf{k}_{p\perp} \int_{-\infty}^{\infty} d\omega_p \\ &\times \chi^2 \sum_{\mathbf{k_s},\mathbf{k}_i} \hat{a}^\dagger_{s,\mathbf{k}_s}\hat{a}^\dagger_{i,\mathbf{k}_i} E_p(\mathbf{k}_{p\perp},\omega_p) e^{i(-\mathbf{k}_s-\mathbf{k}_i+\mathbf{k}_p)\cdot\mathbf{r}} e^{i(\omega_s+\omega_i-\omega_p)t}.\end{aligned} \tag{1.37}$$

When the transverse dimensions of the crystal are large with respect to the beam spot size, the integration over the transverse spatial coordinates can be taken to infinity, giving us

$$\int d\mathbf{r} \quad e^{i(-\mathbf{k}_s-\mathbf{k}_i+\mathbf{k}_p)\cdot\mathbf{r}} = \int_0^L dz \quad \delta(-\mathbf{k}_{s\perp}-\mathbf{k}_{i\perp}+\mathbf{k}_{p\perp})e^{-i(k_{s_z}+k_{i_z}-k_{p_z})z}$$
$$= \delta(-\mathbf{k}_{s\perp}-\mathbf{k}_{i\perp}+\mathbf{k}_{p\perp})e^{-i\Delta kL/2}\left[\frac{\sin(\Delta kL/2)}{(\Delta kL/2)}\right],$$

where $\Delta k = (k_{s_z}+k_{i_z})-k_{p_z}$, and L is the length of the BBO crystal. The integration over transverse wave-vectors for the pump enforces $\mathbf{k}_{s\perp}+\mathbf{k}_{i\perp}=\mathbf{k}_{p\perp}$. This implies conservation of transverse momentum. The interaction Hamiltonian becomes,

$$H_I(t) \propto \int_{-\infty}^{\infty} d\omega_p \sum_{\mathbf{k}_s,\mathbf{k}_i} \hat{a}^\dagger_{s,\mathbf{k}_s}\hat{a}^\dagger_{i,\mathbf{k}_i}E_p(\mathbf{k}_{s\perp}+\mathbf{k}_{i\perp},\omega_p)e^{i(\omega_s+\omega_i-\omega_p)t}e^{-i\Delta kL/2}\left[\frac{\sin(\Delta kL/2)}{(\Delta kL/2)}\right].$$

From the interaction picture, we know that the time evolution of the system is determined by the interaction Hamiltonian, which, to first order, can be approximated as

$$\hat{U}(t) = 1-\frac{i}{\hbar}\int dt' \quad \hat{H}_I(t')$$
$$= 1-\frac{i}{\hbar}\int_{-\infty}^{\infty} d\omega_p \sum_{\mathbf{k}_s,\mathbf{k}_i} \hat{a}^\dagger_{s,\mathbf{k}_s}\hat{a}^\dagger_{i,\mathbf{k}_i}E_p(\mathbf{k}_{s\perp}+\mathbf{k}_{i\perp},\omega_p)\delta(\omega_s+\omega_i-\omega_p)e^{-i\Delta kL/2}\left[\frac{\sin(\Delta kL/2)}{(\Delta kL/2)}\right].$$

Since the SPDC process is inefficient, the time between down-conversions is long hence the time integration is extended over infinity. Lastly, integrating over the pump frequency, ω_p, satisfies conservation of photon energy by enforcing $\omega_p = \omega_s + \omega_i$. Our time evolved state is generated by $|\psi(t)\rangle = \hat{U}(t)\,|0_s, 0_i\rangle$ which gives the biphoton wavefunction

$$\psi(\mathbf{k}_s,\mathbf{k}_i) = \sum_{\mathbf{k}_s,\mathbf{k}_i} E_p(\mathbf{k}_{s\perp}+\mathbf{k}_{i\perp},\omega_p=\omega_s+\omega_i)e^{-i\frac{\Delta kL}{2}}\left[\frac{\sin(\Delta kL/2)}{(\Delta kL/2)}\right]. \tag{1.38}$$

In much of the quantum optics literature, it is customary to approximate the phase-matching contribution containing the Δk term with a Gaussian curve in order to make analytic theoretical calculations tractable. That is an acceptable approximation to make when using thin BBO crystals since the propagation distances within the crystal are small enough that birefringence doesn't cause too many difficulties. However, there has been little research into the new physics that is introduced by taking the full wavefunction into account. This problem will be the primary focus of the article to follow in this thesis.

Figure 1.3: Characteristic single-ring emission pattern observed in type-I spontaneous parametric down-conversion (SPDC). The conical emission of signal and idler photons, determined by momentum and energy conservation together with the crystal phase-matching conditions, produces a circular intensity distribution in the far field. Photon pairs are generated at opposite points on the ring, exhibiting strong spatial and momentum correlations. Image courtesy of the SQO Group.

2

SPDC State Propagation and Entanglement Correlations in the Near-Field

The findings reported in this chapter are based on the publication "Imaging Walk-Off–Driven Distortions in EPR Photon-Pair Correlations" by C. Howard, R. Ghobadi, N. Dehghan, A. D'Errico, and E. Karimi, Optics Express **34***, in press (2026).*

Here, we begin the discussion of the first article presented in this thesis. Spontaneous parametric downconversion (SPDC), as previously mentioned, has been extensively utilized in quantum optics laboratories in the last 30 years. However, almost all of the works presented involve macroscopic propagation distances, where the biphotons propagate paraxially. The exact biphoton wavefunction produced by SPDC is generally difficult to evaluate analytically due to the complexity of the phase-matching function. Consequently, it is common to approximate the biphoton state using a double-Gaussian model, which preserves the essential correlation structure while allowing for analytical treatment. In transverse momentum space, the biphoton wavefunction is expressed as

$$\psi(p_s, p_i) = \sqrt{\frac{AB}{\pi}} \exp\left[-A(p_s + p_i)^2 - B(p_s - p_i)^2\right], \tag{2.1}$$

where p_s and p_i denote the transverse momenta of the signal and idler photons, respectively. The parameters A and B characterize the widths of the sum and difference momentum coordinates and therefore determine the degree of position and momentum correlations exhibited by the photon pair.

As we can see, this wavefunction cannot be written in the form $\psi(p_s, p_i) = \phi_1(p_s)\phi_2(p_i)$ and therefore the wavefunction is entangled in momentum space. Approximations of this sort allow one to separate the wavefunction into a sum and a difference of momentum coordinates, allowing analytic calculations of the state Wigner function, the state Schmidt decomposition, and the modelling of the state propagation. Moreover, the double-Gaussian approximation holds best for the far-field propagation distances typical in quantum optics experiments. Beginning to push forward from the Gaussian approximation scheme, works have also been presented where the wavefunction is approximated with a double-sinc function [44]. However, this neglects the coupling between the sum-coordinates and the phase-matching contribution. Even though the double-Gaussian approximation is mathematically convenient, essential physics is lost, in particular the coupling between the sum-difference coordinates and the phase-matching conditions in the biphoton state. To capture a full picture of how spatial correlations evolve, one must take full account of the bi-photon wavefunction. Little research to date has attempted to take into account the full biphoton wavefunction and examine the new effects introduced, and this is the focus of the coming article. There are many practical scenarios where the separability of sum and difference coordinates breaks down. For example, this occurs in: propagation through large crystals ($L \approx 5mm$), diffraction through out-of-focus elements, propagation through turbulent media (important in the implementation of free-space quantum-optical communication), or in tight-focusing regimes where it is invalid to describe photon propagation with the paraxial wave equation.

Photon pairs generated through type-I SPDC exhibit strong correlations in their transverse spatial degrees of freedom as a direct consequence of energy and momentum conservation during the nonlinear interaction. These spatial correlations give rise to continuous-variable entanglement, making SPDC one of the most versatile sources for quantum information processing, quantum imaging, and quantum communication. Unlike discrete two-level systems, spatial variables provide access to an effectively infinite-dimensional Hilbert space, enabling the encoding and manipulation of large amounts of quantum information. For biphoton states whose wavefunction factorizes in the sum and difference coordinates, the propagation dynamics of spatial entanglement are well understood. At the output face of the nonlinear crystal, the entanglement is primarily manifested through strong position correlations between the signal and idler photons. As photons propagate through free space, diffraction modifies the biphoton wavefunction, thereby causing the observable correlations to evolve. In particular, the entanglement does not remain confined to the intensity distribution but is progressively transferred into the phase structure of the joint state. At intermediate propagation distances, the intensity correlations can appear significantly weakened, leading to the impression that the entanglement has been reduced or even lost. However, this is not the case. The quantum state remains fully entangled throughout propagation, with the entanglement encoded in phase-sensitive correlations that are not directly visible in intensity measurements alone. Upon further propagation toward the far field, the phase structure is converted back into measurable spatial cor-

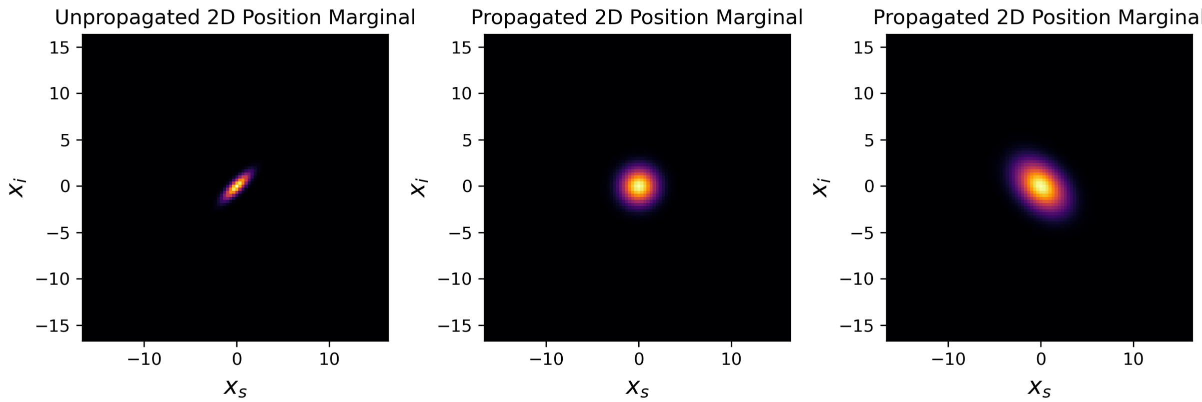

Figure 2.1: The simulated wavefunction is $\psi(p_s, p_i) = \sqrt{\frac{AB}{\pi}} e^{-A(p_s+p_i)^2 - B(p_s-p_i)^2}$, with $A = 30$ and $B = 3$. Strong spatial correlations are observed at the crystal output plane. As the photons propagate, the observable intensity correlations weaken and become nearly absent at $z = 6\,k$, where entanglement is predominantly encoded in the biphoton wavefunction's phase. At longer propagation distances, i.e. $z = 10\,k$, the correlations re-emerge in the intensity distribution, demonstrating the transfer of observable entanglement signatures between the amplitude and phase.

relations. As a result, the initially strong position correlations re-emerge as momentum anti-correlations, consistent with the Fourier-transform relationship between the near- and far-field planes [45]. The apparent disappearance and reappearance of correlations, therefore, reflect not a loss of entanglement, but rather a redistribution of quantum correlations among different degrees of freedom of the biphoton state. The total amount of entanglement remains invariant under free-space propagation, while its manifestation evolves continuously as the joint quantum state undergoes unitary evolution. This entanglement migration between amplitude and phase degrees of freedom provides a striking example of how the physical signature of quantum correlations depends on the measurement basis and propagation geometry.

In our experiment, we demonstrate that accounting for the full biphoton wavefunction reveals novel spatial correlations that have not been captured to date. Those novel correlations arise from the x-bias introduced by the full biphoton wavefunction, producing a wedge-shaped correlation that grows larger as the biphotons separate. To get a better idea of how this all works, let's briefly examine the full-biphoton wavefunction for non-collinear type I SPDC. The full wavefunction is [37]

$$\Phi_0(\mathbf{p}_+, \mathbf{p}_-) = \exp\left\{\frac{-w_+^2 \mathbf{p}_+^2}{4}\right\} \exp\{-i(\beta \mathbf{p}_-^2 + t p_{+,x} - l)\} \,\mathrm{sinc}\{(\beta \mathbf{p}_-^2 + t p_{+,x} - l)\}, \quad (2.2)$$

where the constants t and l represent the transverse and longitudinal walk-off, respectively, with $\beta = \frac{L}{4\eta_p k_p}$ where η_p is the effective refractive index of the pump beam inside the crystal, and sinc(.) is the sinc function. As we know, SPDC is inherently probabilistic, with photon pairs being generated at random locations throughout the nonlinear crystal. In birefringent media such as BBO, the extraordinary pump beam experiences transverse walk-off as it propagates, causing photon pairs generated at different depths within the crystal to emerge from laterally displaced positions. Rather than originating from a single SPDC cone, the detected state can therefore be viewed as the coherent superposition of many slightly shifted emission cones. As these contributions propagate and overlap, they modify the observed spatial correlations, leading to distortions that become increasingly apparent away from the crystal plane. Understanding how these walk-off-induced effects influence the spatial structure of entangled photon pairs is important both from a fundamental and practical perspective. In particular, we are interested in how the correlations evolve for different pump-field geometries, including structured beams carrying orbital angular momentum (OAM). In the conventional Gaussian description of SPDC, an OAM pump generates photon pairs that are entangled in OAM while preserving angular momentum conservation. The corresponding coincidence distribution exhibits the familiar doughnut-shaped structure associated with OAM-carrying fields. An important question is whether the additional correlations introduced by birefringence and propagation can reveal otherwise inaccessible information about the biphoton state and potentially provide new routes toward quantum state reconstruction.

Below, we investigate the propagation of spatially entangled photon pairs generated through SPDC beyond the assumptions commonly employed in standard theoretical treatments. Much of the existing understanding of spatial entanglement in SPDC relies on the thin-crystal approximation, in which the biphoton wavefunction is assumed to factor into independent functions of the sum and difference coordinates. While this approximation has proven highly successful, it neglects the subtle coupling introduced by birefringence-induced transverse walk-off. We show that these effects remain observable even in crystals that nominally satisfy the thin-crystal condition. Through a combination of theoretical analysis, numerical simulations, and experimental measurements, we demonstrate that free-space propagation reveals a previously overlooked coupling between the sum and difference degrees of freedom of the biphoton state. This coupling manifests itself as a characteristic asymmetry in the measured spatial correlations that cannot be captured by conventional factorized models. Beyond providing a more complete description of SPDC, the results presented here highlight the importance of accounting for propagation and birefringence effects when reconstructing, characterizing, and exploiting high-dimensional entangled states for quantum imaging, communication, and information processing.

Research Article | Vol. 34, No. 12 / 15 Jun 2026 / *Optics Express* 22452

Optics EXPRESS

Imaging walk-off–driven distortions in EPR photon-pair correlations

CHRISTIAN HOWARD,[1] ROOHOLLAH GHOBADI,[1] NAZANIN DEHGHAN,[1] ALESSIO D'ERRICO,[1] AND EBRAHIM KARIMI[1,2]

[1]*Nexus for Quantum Technologies, University of Ottawa, Ottawa, ON K1N 5N6, Canada*
[2]*Institute for Quantum Studies, Chapman University, Orange, California 92866, USA*

Abstract: Spontaneous parametric down-conversion is the primary source of position-correlated and momentum–anti-correlated photon pairs that form the canonical Einstein–Podolsky–Rosen (EPR) state. Their transverse spatial correlations are usually analyzed within the thin-crystal approximation, where the two-photon wavefunction is assumed to factorize into independent functions of the sum and difference coordinates. In practice, however, birefringence-induced transverse walk-off breaks this factorization and couples these degrees of freedom. Here, we show that this coupling persists even for nominally thin crystals once the free-space propagation of the joint spatial intensity is taken into account. This sum-difference coordinate coupling leads to a distinctive tapering of the transverse correlations near the crystal image plane – an effect that standard factorized models cannot capture. Numerical simulations and experimental data clearly confirm this novel behavior. Our findings provide a more complete description of photon-pair generation in birefringent nonlinear media and clarify fundamental limits on spatially resolved quantum imaging and spatial-mode quantum information processing with EPR states.

1. Introduction

Spontaneous parametric down-conversion (SPDC) is the most widely used source of entangled photon pairs and has enabled seminal demonstrations of quantum interference [1], entanglement generation [2–4], Einstein–Podolsky–Rosen (EPR) correlations [5], and quantum steering [6]. By providing controllable, high-purity single photons and well-characterized entangled states, SPDC has transformed quantum entanglement from a foundational concept into a practical resource for quantum communication [7,8], imaging [9,10], and photonic quantum information processing [11]. In this sense, SPDC serves as a versatile bridge between fundamental quantum optics and scalable photonic technologies [12].

The theoretical description of SPDC commonly relies on the thin-crystal approximation, in which the biphoton amplitude factorizes into contributions depending on the sum and difference of the transverse coordinates. This separation effectively decouples the pump-envelope function from the phase-matching response and underpins a wide range of analyses, including phase-retrieval and state-reconstruction protocols [13,14], orbital angular momentum (OAM) conservation and engineering [15], and entanglement migration between spatial degrees of freedom [16]. When both the pump and phase-matching functions are further approximated as Gaussians, compact analytical expressions become available for quantifying spatial entanglement through the Schmidt number [17–20] and experimentally accessible estimators such as the Fedorov ratio and EPR variances [1,21,22]. These approximations are well justified in the thin-crystal, small-transverse-walk-off regime, where the phase-matching bandwidth is broad, the pump profile largely determines the joint spatial structure, and non-Gaussian distortions remain negligible.

Free-space propagation, however, can substantially modify how spatial entanglement is distributed among the available degrees of freedom [16,23–26]. More recently, propagation has

#589378 https://doi.org/10.1364/OE.589378
Journal © 2026 Received 5 Jan 2026; revised 29 Apr 2026; accepted 26 May 2026; published 10 Jun 2026

also been exploited as a diagnostic tool to reveal otherwise inaccessible phase information of the biphoton wavefunction and to enable its reconstruction [14]. Building on this perspective, we show here that free-space propagation can likewise expose birefringence induced transverse walk-off effects through a coupling of the transverse sum and difference coordinates. Walk-off effects [27,28] are well known in Type II crystals [29] and have been studied also in the context of thick Type-I crystals [30]. Remarkably, the coupling between sum and difference coordinates can become observable and non-negligible under appropriate conditions, even for relatively thin nonlinear crystals ($L \approx 1$ mm). Specifically, we demonstrate that the resulting non-separability leads to an asymmetric and propagation-dependent broadening of the transverse spatial correlations. We further show that this effect is enhanced when the crystal is pumped with structured light, which amplifies the imprint of walk-off on the joint spatial correlations. We support these findings with heuristic arguments, numerical simulations, and direct experimental observations, and discuss their implications for accurately reconstructing and interpreting the spatial states of biphotons.

2. Theory

We consider a uniaxial nonlinear crystal slab of thickness L, whose optic axis is cut at an angle θ with respect to the propagation direction z of the pump beam. The two-photon wavefunction in the transverse-momentum representation, evaluated at the output face of the crystal ($z = L$), can be written as the product of a pump-envelope contribution and a phase-matching term. We assume a Gaussian pump profile of the form $e^{-w_+^2 \mathbf{p}_+^2/4}$, where w_+ denotes the pump waist at the crystal plane and $\mathbf{p}_\pm = (\mathbf{p}_s \pm \mathbf{p}_i)/\sqrt{2}$, with $\mathbf{p}_s$ and $\mathbf{p}_i$ the transverse momenta of the signal and idler photons, respectively.

The phase-matching function has the general form $e^{-iL\Delta p_z/2}\,\mathrm{sinc}(L\Delta p_z/2)$, where the longitudinal momentum mismatch Δp_z can be expressed in terms of the transverse momentum variables. This leads to the biphoton wavefunction [23]

$$\begin{aligned}\Phi_0(\mathbf{p}_+, \mathbf{p}_-) = {} & e^{-w_+^2 \mathbf{p}_+^2/4}\, e^{-i(\beta \mathbf{p}_-^2 + t p_{+,x} - l)} \\ & \times \mathrm{sinc}(\beta \mathbf{p}_-^2 + t p_{+,x} - l),\end{aligned} \tag{1}$$

where $\beta = L/(4\eta_p k_p)$, with η_p an effective refractive index (see Supplement 1 and Ref. [23]). The parameters t and l represent the transverse and longitudinal walk-off terms, respectively. The longitudinal walk-off arises from the different group velocities of the pump and the down-converted photons, while the transverse walk-off — which is central to this work — originates from the anomalous refraction of the pump beam inside the birefringent crystal, here assumed to be extraordinarily polarized.

A key point is that finite transverse walk-off introduces an explicit dependence of the phase-matching function on the sum coordinate $p_{+,x}$. In the absence of this contribution, the phase matching would depend solely on $\mathbf{p}_-$, and the biphoton wavefunction would factorize in the sum–difference representation as $\Phi_0(\mathbf{p}_+, \mathbf{p}_-) = A_p(\mathbf{p}_+)\,\psi(\mathbf{p}_-)$. This separability is a common assumption and is often taken to be valid in the thin-crystal limit [23]. Only a few works have explicitly addressed the effects of transverse walk-off. In Ref. [31], transverse walk-off was incorporated by approximating the phase-matching function as $\mathrm{sinc}(\beta \mathbf{p}_-^2 + t p_{+,x}) \approx \mathrm{sinc}(\beta \mathbf{p}_-^2)\,\mathrm{sinc}(t p_{+,x})$. For relatively thick crystals ($L = 5$ mm), this approach was shown to accurately describe far-field two-photon correlations, while failing in the near field. Importantly, this approximation, however, restores separability between the sum and difference coordinates. In contrast, we show that the intrinsic coupling between $\mathbf{p}_+$ and $\mathbf{p}_-$ can play a significant role even for relatively thin crystals ($L \sim 1$ mm), where it manifests as pronounced asymmetries in the spatial correlations.

We begin with an intuitive picture that illustrates how coupling in the phase-matching term arises. As sketched in Fig. 1-(a), the extraordinary pump undergoes transverse walk-off inside the crystal, drifting sideways along the optic-axis direction. As a result, photon pairs generated at different longitudinal positions exit the crystal from laterally displaced launch points. Upon free-space propagation to the detection plane, these depth-dependent displacements overlap to form an asymmetric envelope. On the walk-off side, photon pairs generated later in the crystal accumulate into a sharp, tapered edge, whereas on the opposite side, pairs created earlier or near the middle of the crystal spread out more broadly, giving rise to the observed wedge-shaped correlations.

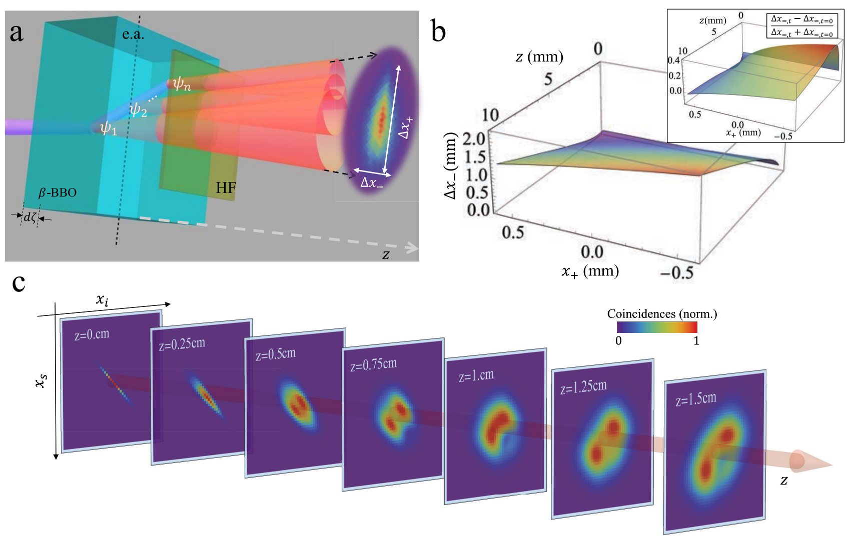

Fig. 1. Birefringence-induced transverse walk-off effects. (a) Schematic illustration of birefringence-induced transverse walk-off in a nonlinear crystal. A pump beam (purple) with a polarization state along extraordinary axes of the crystal undergoes anomalous refraction, causing its centroid to drift laterally along the optic-axis direction as it propagates through the crystal. Consequently, photon pairs, labeled by their wavefunctions ψ_n, and generated within a voxel of thickness $d\zeta$, emerge from laterally displaced locations, leading to a position-dependent width Δx_- of the transverse anti-correlations. HF denotes a high-pass spatial filter. (b) Anti-correlation width Δx_- as a function of propagation distance z and sum coordinate x_+. The inset shows the normalized ratio $\Delta x_-(z, x_+)/\Delta x_-(z, x_+ = 0)$, highlighting that the dependence on x_+ is strongest near the crystal image plane. (c) Simulations of the x-correlations at different propagation distances obtained from Eq. (9).

This behavior can be understood through a simple heuristic argument. The width of the transverse anti-correlation, $\Delta x_-(z)$, measured at a propagation distance z from the crystal, depends on both the initial position width $\Delta x_-(0)$ and the momentum width $\Delta p_-(0)$ evaluated at the crystal plane. For free-space propagation, this dependence follows directly from the ABCD law of geometrical optics, which, expressed in terms of the sum and difference transverse variables $\mathbf{x}_\pm = (\mathbf{x}_s \pm \mathbf{x}_i)/\sqrt{2}$, reads [32]

$$\begin{pmatrix} \mathbf{x}_\pm(z) \\ \mathbf{p}_\pm(z) \end{pmatrix} = \begin{pmatrix} 1 & z/k \\ 0 & 1 \end{pmatrix} \begin{pmatrix} \mathbf{x}_\pm(0) \\ \mathbf{p}_\pm(0) \end{pmatrix}, \tag{2}$$

Optics EXPRESS

where $k = k_s = k_i$ denotes the signal and idler wavenumbers. From this relation, the propagation of the anti-correlation width can be written as

$$\Delta x_-(z) = \sqrt{[\Delta x_-(0)]^2 + (z/k)^2[\Delta p_-(0)]^2}. \tag{3}$$

To estimate $\Delta p_-(0)$, we examine the phase-matching kernel $\mathrm{sinc}(\beta p_-^2 + tp_{+,x} - l)$, which explicitly couples the even p_-^2 term to a linear bias in the sum momentum $p_{+,x}$. Approximating the momentum width by the location of the first zero of the sinc function yields $\Delta p_-(0) = 2\sqrt{(\pi + l - tp_{+,x})/\beta}$. Substituting this into Eq. (3) gives

$$\Delta x_-(z) = \sqrt{[\Delta x_-(0)]^2 + \frac{4z^2}{k^2\beta}(\pi + l - tp_{+,x})}. \tag{4}$$

Using Eq. (2), the sum momentum can be related to the sum coordinate through $p_{+,x} = k[x_+(z) - x_+(0)]/z$. Estimating $x_+(0) \sim w_+/2$ leads to the final expression

$$\Delta x_-(z, x_+) = w_\phi \sqrt{1 + \frac{z^2}{z_{\mathrm{eff}}^2}\left(\pi + l - tk\frac{x_+ - w_+}{z}\right)}, \tag{5}$$

where $w_\phi \equiv \Delta x_-(0)$ and $z_{\mathrm{eff}} = k\sqrt{\beta}\, w_\phi/2$.

In the Gaussian-approximation limit, where walk-off is neglected ($t = 0$, $l \approx 0$) and $\sqrt{\beta} \sim w_\phi$, this expression reduces to the familiar divergence law of Gaussian beams, $w_\phi(z) = w_\phi\sqrt{1 + (z/z_{\mathrm{eff}})^2}$. Finite transverse walk-off introduces an additional correction to the squared anti-correlation width that depends explicitly on the sum coordinate x_+ and grows linearly with propagation distance z to first order, as illustrated in Fig. 1-(b). This correction is responsible for the characteristic wedge-shaped spatial correlations observed experimentally. At large propagation distances, the usual $(z/z_{\mathrm{eff}})^2$ term dominates, rendering the walk-off-induced asymmetry less pronounced. This is evident in the inset of Fig. 1-(b), where we plot the normalized difference $(\Delta x_{-,t} - \Delta x_{-,t=0})/(\Delta x_{-,t} + \Delta x_{-,t=0})$, showing that the effect of finite transverse walk-off is strongest near the crystal image plane. We emphasize that this treatment is qualitative in nature, as it does not fully account for the detailed propagation effects arising from the sinc-shaped phase-matching function.

A first numerical approach, outlined in Supplement 1, is based on evaluating the Wigner function associated with Eq. (1). This approach is limited by the computational power required to evaluate a function of 8 coordinates (the positions and momenta of the idler and signal photons along x and y). However, qualitative results can be obtained by neglecting the y-dependence (Supplement 1 Fig. 1).

To make the comparison with the experiment more quantitative and account for the y dependence, we model the finite crystal as a coherent sum of thin longitudinal emitters. The crystal is subdivided into M slices of thickness $d\zeta = L/M$ (voxels), and each slice emits a Gaussian biphoton amplitude satisfying the thin-crystal approximation. The total biphoton wavefunction is obtained by the superposition of the biphoton states generated from each voxel

$$\Phi_0(\mathbf{r}_i, \mathbf{r}_s) = \sum_{n=1}^{M} \psi_n(\mathbf{r}_i, \mathbf{r}_s), \tag{6}$$

where n refers to the n^{th} volume element of the crystal. We can now resort to the double Gaussian approximation since, within each voxel, the thin crystal approximation is well satisfied. The walk-off is accounted for by introducing a lateral displacement $x_{0,n}$ in the pump contribution, which depends on the position within the crystal: $x_{0,n} = \varrho\, n\, d\zeta$, with $\varrho \approx t/L$ being the transverse walk-off angle. The bi-photon state emitted from the n^{th} volume element is thus

$$\psi_n(\mathbf{r}_i, \mathbf{r}_s) = e^{-\frac{(x_+ + 2x_{0,n})^2}{w_+^2}} e^{-\frac{y_+^2}{w_+^2}} e^{-\frac{x_-^2 + y_-^2}{w_-^2}}, \tag{7}$$

where the phase matching width is $w_- \approx \sqrt{\beta\, d\zeta / L}$. It is important to note that, in order to use the paraxial approximation, we are constrained to use a number of voxels M such that $w_- \gg \lambda_p$. The wavefunctions at a distance z can now be analytically calculated from standard Gaussian beam results, in particular introducing the q-parameters $q_\pm(z) = z + i\pi w_\pm^2/\lambda_p$, and the notation $q_{\pm,n} := q_\pm(z - n\, d\zeta)$ – note that the propagation along the sum and difference coordinates is dictated by the pump wavelength [14] –. The propagated voxel wavefunction is

$$\psi_n(\mathbf{r}_i, \mathbf{r}_s, z) = \frac{1}{q_{+,n} q_{-,n}} e^{-i\frac{k}{2q_{+,n}}[(x_+ + 2x_{0,n})^2 + y_+^2]} e^{-i\frac{k}{2q_{-,n}}(x_-^2 + y_-^2)}, \tag{8}$$

where the dependence on z is encoded in the q parameters.

We calculate the x-correlations as $C(x_+, x_-, z) := \int |\Phi_0(\mathbf{r}_i, \mathbf{r}_s, z)|^2 dy_+ dy_-$. After writing the square modulus explicitly and solving the Gaussian integrals along $y_\pm$, we finally obtain

$$\begin{aligned} C(x_+, x_-, z) \propto \sum_{m,n} & \frac{e^{i\delta(m-n)}}{[(q_{+,m}^* - q_{+,n})(q_{-,m}^* - q_{-,n}) q_{+,n} q_{-,n} q_{+,m}^* q_{-,m}^*]^{1/2}} \\ & \times \exp\left[-\frac{ik}{2}\left(\frac{(x_+ + 2x_{0,n})^2}{q_{+,n}} - \frac{(x_+ + 2x_{0,m})^2}{q_{+,m}^*} + \left(\frac{1}{q_{-,n}} - \frac{1}{q_{-,m}^*} \right) x_-^2 \right) \right], \end{aligned} \tag{9}$$

where δ is the phase mismatch between pump and SPDC accumulated in the crystal. Figure 1-c shows the simulations according to Eq. (9) where we choose parameters close to our experiment: $w_+ = 0.2$ mm, $L = 1.68$ mm – the length was corrected by the crystal's tilt –, $d\zeta = L/6$, $w_- = 6\,\mu$m, $\lambda_p = 405$ nm.

3. Experiment

We experimentally verified the predicted effects of transverse walk-off by measuring the evolution of spatial correlations in SPDC generated from a 1-mm-thick type-I BBO crystal pumped by a pulsed 405-nm laser. The pump beam was focused onto the crystal, with a measured waist of approximately 0.2 mm at the crystal plane, which satisfies the thin crystal approximation, i.e. $L/z_R \simeq 3 \times 10^{-3}$. The experimental setup is schematically shown in Fig. 2-(a). After the crystal, an imaging system with 4× magnification was used to measure near-field spatial correlations using an event-based camera (Tpx3Cam) [33,34]. Signal and idler photons were spatially separated, with 50% probability, so as to impinge on two distinct regions of the camera sensor. This separation was achieved using a half-wave plate rotated by 22.5° followed by two polarizing beam splitters, arranged such that both photons propagate over equal optical path lengths (see Ref. [14] for further details).

Spatial correlations were recorded at different propagation distances z, referenced to the image plane of the crystal ($z = 0$). The $z = 0$ position was identified as the plane where the two-photon spatial correlations were the sharpest. The rapid acquisition time and data analysis allows to observe these correlations in real time –with updates on the correlation patterns every few seconds– thus allowing us to precisely identify the source plane with an uncertainty of the order of the crystal's thickness. Measurements were performed for propagation distances ranging from $z = 0$ to 15 mm in steps of 2.5 mm. The experimentally reconstructed spatial correlations clearly reveal the characteristic wedge-shaped structure predicted by our model (see Fig. 2-(b)), which is particularly pronounced at intermediate propagation distances. Overall, the experimental

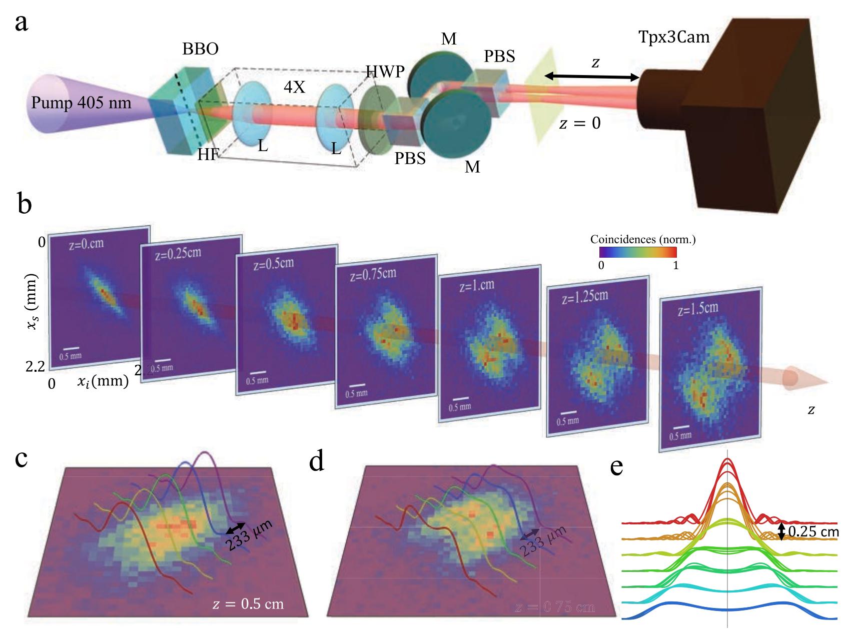

Fig. 2. **Experimental results.** (a) Schematic of the experimental setup. BBO: 1-mm-thick type-I β-barium borate crystal; HF: high-pass filter; L: lens; HWP: half-wave plate; PBS: polarizing beamsplitter; M: mirror. (b) Experimentally reconstructed transverse spatial correlations along the x coordinate. (c,d) Detailed analysis of transverse walk-off effects, highlighting the dependence of the correlation width on the sum coordinate x_+. The one-dimensional cuts show best fits of the coincidence distributions for fixed values of $x_i - x_s$, sampled in steps of 233 μm, illustrating how the spatial correlations evolve along this direction due to transverse walk-off. (f) Same one-dimensional analysis as in (d,e), shown for all measured propagation planes. When stacked together, these reconstructed profiles map out the free-space propagation of the phase-matching function.

observations are in good agreement with the numerical simulations as certified by the evaluation of the Similarity S between theory and experiment. The similarity is defined as $S = \sqrt{\mathbf{e}.\mathbf{t}}$, where $\mathbf{e}$ ($\mathbf{t}$) are vectors obtained by normalizing and flattening the experimental (theoretical) results. We obtain $S = 0.75$, 0.8, 0.96, 0.97, 0.95, 0.97, and 0.96.

A more detailed analysis of selected cases is presented in Fig. 2-(d) and (e), corresponding to propagation distances of $z = 5$ mm and $z = 7.5$ mm, respectively. The colored curves represent fits to one-dimensional sections of the coincidence distributions taken along lines defined by $x_i = -x_s + c$, where c is a variable offset parameter. The fits were performed using a $\mathrm{sinc}^2(Ax^2 - B)$ functional form, with A and B as fitting parameters. Although this expression does not provide an exact analytical description of the phase-matching function at intermediate propagation planes, it serves as an effective phenomenological model (see Supplement 1 Fig. 2), as it can reproduce both Gaussian-like and double-lobed profiles. In Fig. 2-(d), the progressive broadening of the fitted sections with increasing c–corresponding to a transition from the purple to the red curves–directly reflects the influence of transverse walk-off. In Fig. 2-(e), one can additionally observe the emergence of a pronounced double-lobed structure for larger values of c. This evolution closely resembles the free-space propagation of the phase-matching function in the absence of transverse walk-off ($t = 0$), an analogy that becomes more evident when comparing measurements taken at different propagation planes, as shown in Fig. 2-(f).

Transverse walk-off effects become even more apparent when the crystal is illuminated with structured pump beams. As a representative example, we consider a pump beam carrying an azimuthal phase factor $e^{i\ell\phi}$, corresponding to an orbital angular momentum (OAM) of $\ell\hbar$ per photon. Figure 3-(a) shows the measured spatial correlations at a propagation distance of 20 mm from the crystal image plane, where a distinctly triangular structure emerges in the x-correlations. In the absence of transverse walk-off, the pump spatial profile can be reconstructed by post-selecting on correlated photon pairs [14]. This is possible because the separability of the biphoton wavefunction in the sum and difference coordinates allows the pump and phase-matching contributions to be independently extracted from coincidence measurements. When transverse walk-off is non-negligible, however, information about the pump profile is not lost; instead, it becomes intrinsically coupled to the phase-matching function. Consequently, post-selection on spatially correlated events defined by $x_i = x_s + c$ yields results that depend explicitly on the chosen value of c, as illustrated in Fig. 3-(b). In all cases, the characteristic doughnut-shaped intensity profile associated with OAM beams remains visible, but it acquires a pronounced asymmetry due to its convolution with the phase-matching response. This example also illustrates how the walk-off leads to violations of OAM conservation, as highlighted in a recent work [35].

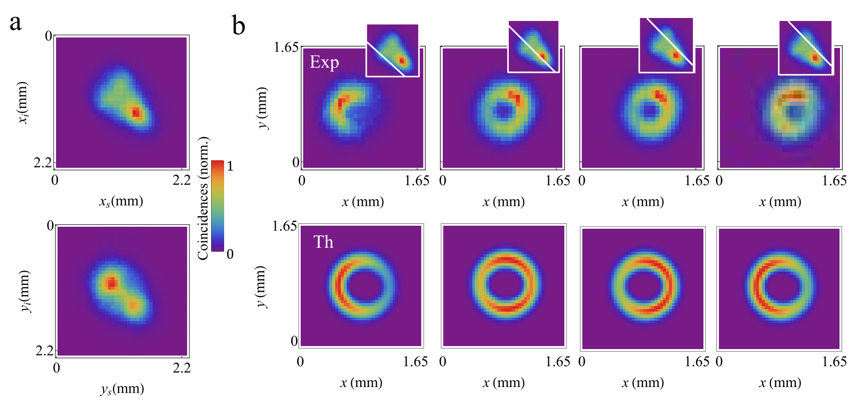

Fig. 3. Transverse walk-off effects with OAM pumping. (a) Measured transverse spatial correlations at a propagation distance of $z = 20$ mm when the crystal is pumped with a beam carrying orbital angular momentum $\ell = 6$. Transverse walk-off effects are particularly evident in the x-correlations, where they introduce pronounced asymmetries. (b) Coincidence images obtained by post-selecting on spatially correlated photon pairs satisfying $x_i = x_s + c$. In the absence of transverse walk-off, this procedure would directly reconstruct the pump intensity profile. When a walk-off is present, however, the reconstructed intensity becomes dependent on the post-selection condition, as highlighted in the insets. The rectangular bars indicate the different values of c used for post-selection. The lower figures in panel (b) show the simulations obtained from Eq. (11).

The experimental results in Fig. 3-(b) can be calculated in light of the theory developed in the previous section. For a structured pump, the voxel wavefunctions should be modified as

$$\psi_n(\mathbf{r}_i, \mathbf{r}_s, z) = P_n(x_+ + 2x_{0,n},\, y_+,\, z)\frac{1}{q_{-,n}} e^{-i\frac{k}{2q_{-,n}}(x_-^2+y_-^2)}, \tag{10}$$

Optics EXPRESS

where P_n is the pump amplitude propagated to the plane z starting from the n-th voxel. The measured correlation images can be calculated from

$$\Gamma_c(x \equiv x_i, y \equiv y_i) = \sum_{c'} |\Phi_0(x_i = x_s + c, y_i = y_s + c', z)|^2, \tag{11}$$

where Φ_0 is calculated from Eq. (6), and the sum over c' is equivalent to consider that no post-selection is applied in the y-coordinates. For the simulations in Fig. 3-b we described the pump wavefunction as an Hypergeometric-Gaussian mode [36] $P(x, y, z) = \mathrm{HyGG}_{-|\ell|,\ell}(x, y, z)$ carrying OAM $\ell = 6$. The post-selection dependent asymmetry that we observed experimentally is well reproduced by this model. Deviations from the experiment are likely due to the low resolution of the acquired images, which are effectively convolved with the pixel size. In the Supplement 1 Figure S3, we show the comparison between experiment and theory, where a Gaussian filter is applied to the theoretical results.

4. Conclusions

In conclusion, we have shown that transverse walk-off induces an intrinsic coupling between the pump and phase-matching contributions, leading to asymmetric and propagation dependent modulations of the joint position-space coincidence distribution. The resulting wedge-shaped spatial correlations constitute a previously unexplored effect that must be taken into account in quantum imaging and state-reconstruction experiments that rely on propagation-dependent measurements. Although transverse walk-off can degrade the direct interpretation of spatial correlations, our results demonstrate that a careful analysis based on coincidence post-selection can still be used to retrieve meaningful information about the constituent functions of the two-photon state. An interesting direction for future work is the investigation of these effects in the high-gain parametric down-conversion regime, where multimode dynamics may further enhance or modify the observed behavior.

More broadly, the approach presented here can be generalized to other scenarios in which the separability of the biphoton wavefunction in sum and difference coordinates breaks down during propagation [31,37,38]. Relevant examples include diffraction through out-of-focus objects, propagation through turbulent or scattering media [39,40], and tight-focusing regimes where the paraxial approximation is no longer valid [41]. In these contexts, propagation-induced coupling between spatial degrees of freedom may provide both challenges and new opportunities for controlling and exploiting high-dimensional quantum correlations.

Funding. Canada Research Chairs; National Research Council Canada Quantum Sensing Program; Quantum Enhanced Sensing, Imaging (QuEnSI); Alliance Consortia Quantum grant.

Acknowledgment. The authors acknowledge discussion with Yingwen Zhang.

Disclosures. The authors declare that they have no competing interests.

Author contributions. R. G., A. D., and C. H. developed the heuristic description of the walk-off effects. A. D., with contributions from C. H. and R. G., developed the semi-analytical theory. C. H. and A. D. performed the numerical simulations. N. D. and A. D. prepared the experimental setup. A. D., with contributions from C. H. and R. G., performed the experiment and analyzed the data. N. D. and A. D. collected the data for the OAM pump. E. K. supervised the project. R. G., A. D., and C. H. prepared the first version of the manuscript.

Data availability. All data are available upon reasonable request to the corresponding authors.

Supplemental document. See Supplement 1 for supporting content.

References

1. C.-K. Hong, Z.-Y. Ou, and L. Mandel, “Measurement of subpicosecond time intervals between two photons by interference,” Phys. Rev. Lett. **59**(18), 2044–2046 (1987).
2. Y. Shih and C. O. Alley, “New type of einstein–podolsky–rosen–bohm experiment using pairs of light quanta produced by optical parametric down conversion,” Phys. Rev. Lett. **61**(26), 2921–2924 (1988).

Optics EXPRESS

3. P. G. Kwiat, K. Mattle, H. Weinfurter, *et al.*, "New high–intensity source of polarization–entangled photon pairs," Phys. Rev. Lett. **75**(24), 4337–4341 (1995).
4. G. Weihs, T. Jennewein, C. Simon, *et al.*, "Violation of bell's inequality under strict einstein locality conditions," Phys. Rev. Lett. **81**(23), 5039–5043 (1998).
5. J. C. Howell, R. S. Bennink, S. J. Bentley, *et al.*, "Realization of the einstein–podolsky–rosen paradox using momentum and position–entangled photons from spontaneous parametric down conversion," Phys. Rev. Lett. **92**(21), 210403 (2004).
6. D. J. Saunders, S. J. Jones, H. M. Wiseman, *et al.*, "Experimental epr–steering using bell–local states," Nat. Phys. **6**(11), 845–849 (2010).
7. Z.-S. Yuan, X.-H. Bao, C.-Y. Lu, *et al.*, "Entangled photons and quantum communication," Phys. Rep. **497**(1), 1–40 (2010).
8. L. Scarfe, Y. Zhang, and E. Karimi, "Spatial–mode quantum cryptography in a 545–dimensional hilbert space," arXiv (2025).https://arxiv.org/html/2503.22058v1
9. T. B. Pittman, Y. H. Shih, D. V. Strekalov, *et al.*, "Optical imaging by means of two–photon quantum entanglement," Phys. Rev. A **52**(5), R3429–R3432 (1995).
10. P.-A. Moreau, E. Toninelli, T. Gregory, *et al.*, "Imaging with quantum states of light," Nat. Rev. Phys. **1**(6), 367–380 (2019).
11. S. Slussarenko and G. J. Pryde, "Photonic quantum information processing: A concise review," Appl. Phys. Rev. **6**(4), 041303 (2019).
12. J. L. O'brien, A. Furusawa, and J. Vučković, "Photonic quantum technologies," Nat. Photonics **3**(12), 687–695 (2009).
13. G. Ortolano, A. Paniate, P. Boucher, *et al.*, "Quantum enhanced non–interferometric quantitative phase imaging," Light: Sci. Appl. **12**(1), 171 (2023).
14. N. Dehghan, A. D'Errico, F. Di Colandrea, *et al.*, "Biphoton state reconstruction via phase retrieval methods," Optica **11**(8), 1115–1123 (2024).
15. A. Mair, A. Vaziri, G. Weihs, *et al.*, "Entanglement of the orbital angular momentum states of photons," Nature **412**(6844), 313–316 (2001).
16. K. Chan, J. Torres, and J. Eberly, "Transverse entanglement migration in hilbert space," Phys. Rev. A **75**(5), 050101 (2007).
17. A. Ekert and P. L. Knight, "Entangled quantum systems and the schmidt decomposition," Am. J. Phys. **63**(5), 415–423 (1995).
18. S. Parker, S. Bose, and M. Plenio, "Entanglement quantification and purification in continuous–variable systems," Phys. Rev. A **61**(3), 032305 (2000).
19. C. Law and J. Eberly, "Analysis and interpretation of high transverse entanglement in optical parametric down conversion," Phys. Rev. Lett. **92**(12), 127903 (2004).
20. F. M. Miatto, H. di Lorenzo Pires, S. M. Barnett, *et al.*, "Spatial schmidt modes generated in parametric down–conversion," Eur. Phys. J. D **66**(10), 263 (2012).
21. M. Fedorov, M. Efremov, P. Volkov, *et al.*, "Short–pulse or strong–field breakup processes: a route to study entangled wave packets," J. Phys. B: At., Mol. Opt. Phys. **39**(13), S467–S483 (2006).
22. E. Gómez, W. Nogueira, C. Monken, *et al.*, "Quantifying the non–gaussianity of the state of spatially correlated down–converted photons," Opt. Express **20**(4), 3753–3772 (2012).
23. S. P. Walborn, C. Monken, S. Pádua, *et al.*, "Spatial correlations in parametric down–conversion," Phys. Rep. **495**(4-5), 87–139 (2010).
24. D. Tasca, S. Walborn, P. Souto Ribeiro, *et al.*, "Detection of transverse entanglement in phase space," Phys. Rev. A **78**(1), 010304 (2008).
25. D. Tasca, S. Walborn, P. Souto Ribeiro, *et al.*, "Propagation of transverse intensity correlations of a two–photon state," Phys. Rev. A **79**(3), 033801 (2009).
26. A. Bhattacharjee, M. K. Joshi, S. Karan, *et al.*, "Propagation–induced revival of entanglement in the angle–oam bases," Sci. Adv. **8**(31), eabn7876 (2022).
27. M. H. Rubin, "Transverse correlation in optical spontaneous parametric down-conversion," Phys. Rev. A **54**(6), 5349–5360 (1996).
28. T. E. Keller and M. H. Rubin, "Theory of two-photon entanglement for spontaneous parametric down-conversion driven by a narrow pump pulse," Phys. Rev. A **56**(2), 1534–1541 (1997).
29. G. Brida, M. Genovese, M. V. Chekhova, *et al.*, "Tailoring polarization entanglement in anisotropy-compensated spontaneous parametric down-conversion," Phys. Rev. A **77**(1), 015805 (2008).
30. L. Coccia, A. Santamato, G. Vallone, *et al.*, "Optimal focusing conditions for bright spontaneous parametric down-conversion sources," Phys. Rev. A **107**(6), 063712 (2023).
31. A. da Costa Moura and C. Monken, "Einstein–podolsky–rosen correlations in spontaneous parametric down–conversion: Beyond the gaussian approximation," Phys. Rev. A **110**(3), 033713 (2024).
32. G. R. Fowles, *Introduction to modern optics* (Courier Corporation, 1989).
33. A. Nomerotski, "Imaging and time stamping of photons with nanosecond resolution in timepix based optical cameras," Nucl. Instrum. Methods Phys. Res., Sect. A **937**, 26–30 (2019).

34. A. Nomerotski, M. Chekhlov, D. Dolzhenko, *et al.*, "Intensified Tpx3Cam, a fast data-driven optical camera with nanosecond timing resolution for single photon detection in quantum applications," J. Instrum. **18**(01), C01023 (2023).
35. Y. Xu and R. W. Boyd, "Engineering walk-off-induced orbital angular momentum spectrum in spontaneous parametric downconversion," Opt. Lett. **51**(7), 1804–1807 (2026).
36. E. Karimi, G. Zito, B. Piccirillo, *et al.*, "Hypergeometric-gaussian modes," Opt. Lett. **32**(21), 3053–3055 (2007).
37. H. Di Lorenzo Pires and M. van Exter, "Near–field correlations in the two–photon field," Phys. Rev. A **80**(5), 053820 (2009).
38. B. Baghdasaryan, F. Steinlechner, and S. Fritzsche, "Maximizing the validity of the gaussian approximation for the biphoton state from parametric down–conversion," Phys. Rev. A **106**(6), 063714 (2022).
39. A. K. Jha, G. A. Tyler, and R. W. Boyd, "Effects of atmospheric turbulence on the entanglement of spatial two–qubit states," Phys. Rev. A **81**(5), 053832 (2010).
40. P. Cameron, B. Courme, C. Vernière, *et al.*, "Adaptive optical imaging with entangled photons," Science **383**(6687), 1142–1148 (2024).
41. A. Vega, E. A. Santos, J. Fuenzalida, *et al.*, "Fundamental resolution limit of quantum imaging with undetected photons," Phys. Rev. Res. **4**(3), 033252 (2022).

IMAGING WALK-OFF--DRIVEN DISTORTIONS IN EPR PHOTON-PAIR CORRELATIONS: SUPPLEMENTAL DOCUMENT

S1. DEPENDENCE OF BIPHOTON WAVEFUNCTION PARAMETERS ON REFRACTIVE INDICES AND CRYSTAL ORIENTATION

The parameters t, l and η_p in Eq. (1) can be expressed in terms of refractive indices and the crystal orientation θ as:

$$t = \frac{L(n_o^2 - n_e^2)\sin\theta\cos\theta}{2n^2(\theta)},$$
$$l = \frac{Lk_p(\eta_p - \overline{n})}{2},\ \eta_p = \frac{n_o n_e}{n(\theta)},$$
$$n^2(\theta) = n_o^2 \sin\theta^2 + n_e^2 \cos\theta^2\ ,\overline{n} = \frac{n_o + n_e}{2} \quad \text{(S1)}$$

where n_o and n_e are the ordinary and extraordinary refractive indices, respectively, at the pump wavelength. In what follows, we focus on frequency degenerate SPDC, wherein the signal and idler have identical frequencies; the results extend straightforwardly to the non-degenerate regime.

S2. WIGNER FUNCTION APPROACH

The first approach is based on calculating the Wigner function of the biphoton state, defined as

$$\begin{aligned} &W(x_+.x_-;p_+,p_-) \\ &= \iint \frac{d\,q_+ dq_-}{(2\pi)^4}\ e^{i(x_+q_+ + x_-q_-)} \\ &\times \Phi_0\left(p_+ + \frac{q_+}{2}, p_- + \frac{q_-}{2}\right) \times \Phi_0^*\left(p_+ - \frac{q_+}{2}, p_- - \frac{q_-}{2}\right) \end{aligned}$$

Under the linear transformation in Eq. 2 the free-space evolution of the Wigner function takes a particularly simple form

$$W\left(x_\pm(z), p_\pm(z)\right) = W(x_\pm \pm z\frac{p_\pm}{k}, p_\pm)$$

We used this result to propagate the Wigner function through free space. Specifically, we first calculate the initial Wigner function corresponding to the biphoton state in Eq.1 using the parameters $w_+ = 50$, $\beta = 1$, $t = 4.0$, and l = 3.0. The propagation is implemented by transforming the phase-space axes and interpolating the Wigner function onto the new coordinate grid. By integrating $W(p_i(z), p_s(z), x_i(z), x_s(z))$ over the momentum variables $(p_i(z), p_s(z))$, we obtain the position-space marginal probability distribution, which is proportional to the experimentally measured spatial correlations at distance z.

% The resulting transverse spatial correlations for several propagation planes are shown in Fig. S2. The simulations reveal the characteristic emergence of a right-diagonal lobe, whose broader end is aligned along the line $x_i = x_s$ which becomes increasingly pronounced with propagation distance.

The numerical computation of the Wigner function for the biphoton state is performed in Python using the NumPy and Matplotlib libraries. In order to compute the Wigner function we take the Fourier Transform of the argument $\Phi(p - p_0/2)\ \Phi^*(p + p_0/2)$ with respect to p_0. Therefore, to model the propagation of the biphoton Wigner function, we numerically compute the Wigner function using iterated Fast Fourier Transforms. We now present an outline of the program's construction.

Pick a real number P > 0 and consider the set S = (-P, P) × (-P, P) ⊂ ℝ × ℝ. The real number P should be large enough so that the support of $\Phi(p - p_0/2)\ \Phi^*(p + p_0/2)$ is contained in S. We then construct a uniform partition P of the set S into N × N cells. We then sample the midpoint of each of the cells in P to get the set of sampled momentum space coordinates s = {(ps_n, pi_m) = (-P + P(1+2n)/N, -P + P(1+2m)/N) : n, m = 0, ..., N - 1}.

Then for each fixed $p_{n,m} = (p_{sn}, p_{im}) \in s$, we compute the Fast Fourier Transform to get $W(x_s, x_i, p_{sn}, p_{im}) = FFT\{\Phi(p_{nm} - p_0/2)\,\Phi*\,(p_{nm} + p_0/2)\}$. The numerical Wigner function is then constructed by taking the set of all such $W(x_s, x_i, p_{sn}, p_{im})$. Hence the numerical Wigner function is the set $W(x_s, x_i, p_s, p_i) = \{W(x_s, x_i, p_{sn}, p_{im}) : n, m = 0, \ldots, N - 1\}$.

We realize the propagation of our Wigner function through a passive transformation of the position and momentum axes. Finally, we obtain our propagated position marginal distribution by numerically integrating over the momentum space variables (p_s, p_i).

In our simulations, the momentum space {p_0 : p_0 = (p_s0, p_i0)} is discretized into an M × M grid centered about the origin where M = 124. The position space, $\{x : x = (x_s, x_i)\}$, which corresponds to the Fourier plane, will also be discretized into an M × M grid by the Fast Fourier Transform. The momentum space, $\{p : p = (p_s, p_i)\}$ is discretized into an N × N grid where N = 1.5 M = 186. The propagation parameter, μ, is allowed to take on the following set of values {0.0, 0.25, 0.5, 0.75, 1.0, 1.25, 1.50}.

We observe that for μ = 0, which corresponds to the position marginal at the exit face of the crystal, we see very tight correlations along the main diagonal. In the case for zero transverse walk-off (t = 0) we see that as we propagate the transverse plane, the position marginal transitions from being dominant along the correlation diagonal to becoming dominant along the anti-correlation diagonal.

In the simulations with non-zero transverse walk-off (t = 4.0) and longitudinal walk-off (l = 3.0), we observe the characteristic formation of a diagonal pointing lobe. As the propagation distance increases, we observe fictitious fringes that are simple artifacts of a lack of resolution in the position and momentum spaces. These fringes are ruled out by the 4D theory presented in the main.

On the other hand, in the simulations with walk-off, we see that upon propagation, our position marginal distribution obtains a lobe shape whose wide end is directed along the correlation diagonal $x_i = x_s$. This means initially, we are nearly certain to detect the two photons having the same position, which makes sense since photons are generated from the same pump photon at a specific location within the BBO crystal. Then, upon propagation, we observe the transverse walk-off as it becomes more likely to detect the two photons farther apart from one another.

S3. SUPPLEMENTARY FIGURES

Figure S1 shows the results of the x-correlations based on the Wigner function approach.

Figure S2 compares the experimental data with the corresponding best fits that are shown in Fig. 2-(c)-(e) for all propagation planes and transverse sections considered.

Figure S3 compares the experimental correlation images with the OAM-carrying pump and the theory with an applied Gaussian filter (with width=10 pixels in Fourier space).

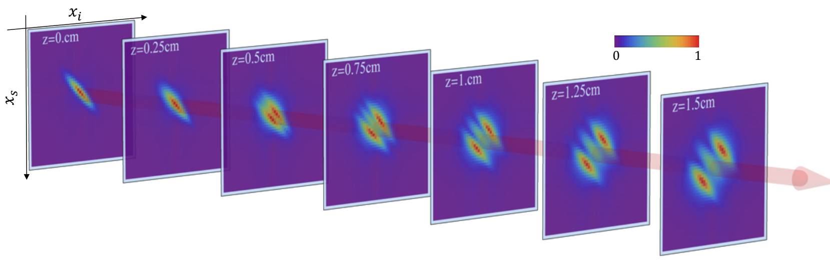

Fig. S1. Evolution of spatial correlations according to Wigner function propagation.

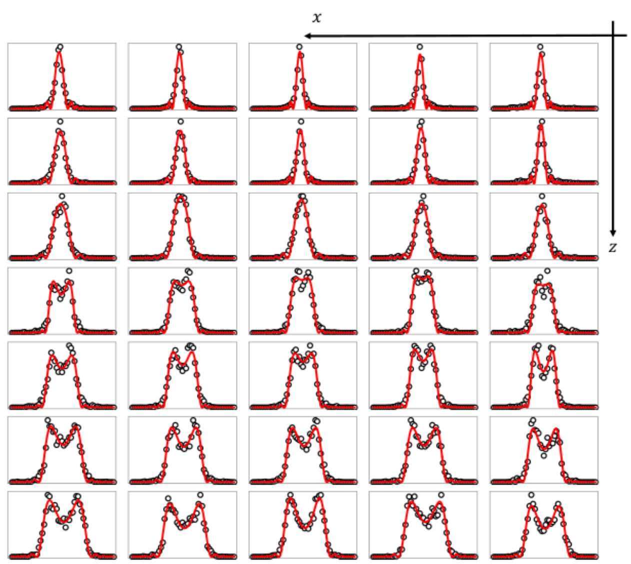

Fig. S2. Fits of sections of measured correlation patterns. Full comparison between experimental data (black circles) and best fits (red plots) that was shown in Fig. 2-(c)-(e) for all propagation planes and sections considered. The R^2 correlation coefficient varies between 95% and 99%.

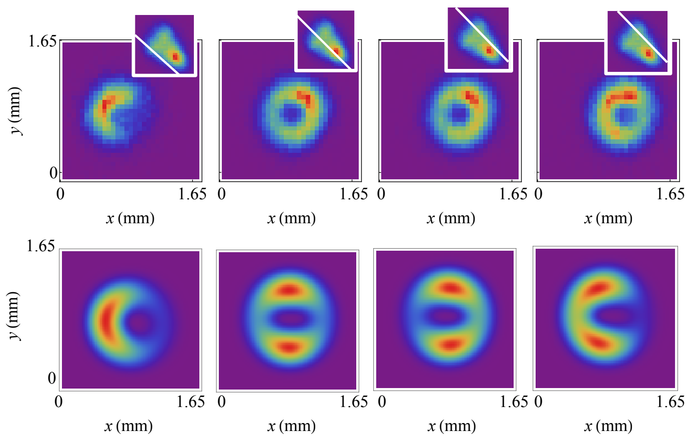

Fig. S3. Results from Figure 3-(b) with a Gaussian filter applied on the theoretical results (bottom row) to simulate the effect of the limited camera resolution.

3

Nonparaxial Evolution of OAM-Entangled Photon Pairs

Diffraction is one of the most fundamental phenomena associated with wave propagation. It describes the tendency of a wave to deviate from straight-line motion when it encounters an obstacle or passes through an aperture. First systematically studied by Francesco Maria Grimaldi in the seventeenth century. Diffraction later became a cornerstone of wave optics and provided compelling evidence for the wave nature of light. Studies by Huygens, Young, and Fresnel established diffraction as a fundamental mechanism underlying light focusing and image formation. Today, diffraction underlies many of the most important processes in optics, including light focusing and image formation. In many optical systems, light propagation can be accurately described within the paraxial approximation, which assumes that rays propagate at small angles relative to the optical axis, see paraxial wave equation approximation in chapter 1. This approximation is sufficient for a wide range of laboratory and everyday applications. However, a complete description of light propagation requires solutions of the full Helmholtz equation. Such solutions were introduced earlier through the angular spectrum representation of the electromagnetic field and became particularly important for strongly focused beams and large propagation angles. The study of non-paraxial light has led to significant advances across modern optics. Notable examples include near-field optical microscopy, where non-paraxial fields enable imaging and characterization of materials with subwavelength resolution, providing access to physical processes at atomic and molecular scales. Understanding the behavior of tightly focused light is therefore essential in many areas of contemporary photonics and optical engineering. To determine the electromagnetic field in the focal region of a high numerical aperture (NA) objective, one must solve Maxwell's equations subject to the appropriate boundary conditions at the interface between the lens and the surrounding medium. The first rigorous treatment of this problem was developed by Richards and Wolf in their seminal 1959 work on electromagnetic diffraction through an aplanatic optical system [46, 47]. Their formalism remains the foundation for describing tightly focused electromagnetic fields.

To derive the electric field in the focus of a large numerical aperture (NA) system we start from the angular spectrum representation, which relates the Fourier transform of the focal field to the field at some distance z. What we need to do is establish a relationship between the Fourier-transformed field in the focal region and the Fourier-transformed field over the lens. This is accomplished by evaluating the angular spectrum representation integral at a point at infinity by the method of stationary phase which when carried out yields,

$$\mathbf{E}(x, y, z) = \frac{ife^{-ikf}}{2\pi} \iint \mathbf{TE}_{\text{in}}(k_x, k_y) e^{i(k_x x + k_y y \pm k_z z)} \frac{1}{k_z} dk_x dk_y. \tag{3.1}$$

Where $\mathbf{TE}_{\text{in}}(k_x, k_y)$ is the linear transformation representing the refraction of incoming rays on the focusing objective. Then we make a change of variables into cylindrical coordinates where $(x, y, z) \mapsto (\rho, \varphi, z)$ and convert the integration into k-space spherical coordinates,

$$k_x = k \sin\theta \cos\phi \tag{3.2}$$

$$k_y = k \sin\theta \sin\phi \tag{3.3}$$

$$k_z = k \cos\theta, \tag{3.4}$$

where $\phi \in [0, 2\pi]$ and $\theta \in [0, \alpha]$ where $\alpha = \arcsin\left(\frac{\mathrm{NA}}{n}\right)$ is the maximum polar angle of the lens. This change of variables can be seen by examining Figure 3.1 and 3.2 where a ray traveling along the optic axis is refracted radially towards the origin. Putting these results together and we arrive at the Richards-Wolf integral of tight-focusing,

$$\mathbf{E}(\rho, \varphi, z) = \frac{-ifk}{2\pi} e^{-ifk} \int_0^{\alpha} \int_0^{2\pi} \mathbf{T}\mathbf{E}_{\mathrm{in}}(\theta, \phi)\, e^{ikz\cos\theta + ik\rho\sin\theta\cos(\phi-\varphi)}\, \sin\theta\, d\phi\, d\theta. \tag{3.5}$$

Lastly we must establish the ray transfer matrix $\mathbf{T}$ that governs the refraction of the incoming beam on the focusing objective. Consider a cylindrical vector beam propagating along the positive-z axis toward a spherical lens. We describe the transverse field using the cylindrical basis vectors $\{\vec{\rho}, \vec{\phi}\}$ and assume that the incident beam completely fills the entrance pupil of the lens. Prior to refraction, the rays propagate parallel to the optical axis. Upon passing through a lens of focal length f, they are redirected toward the focal point located at $z = 0$. The azimuthal basis vector $\vec{\phi}$ remains invariant since it is always tangent to the surface of the spherical lens. The radial basis vector is mapped into the polar tangent vector on the spherical lens. For a ray entering the lens at a radial distance h from the optical axis, the geometry of the aplanatic system yields $h = f \sin\theta$, where θ is the convergence angle of the refracted ray. If the incident beam possesses a transverse electric field distribution $\mathbf{E}_{\mathrm{in}}$, the action of the lens can be described by a transfer matrix that accounts for the refraction and polarization transformation of the field [48, 49, 50],

$$\mathbf{T} = \sqrt{\cos\theta} \begin{bmatrix} \cos\theta\cos^2\phi + \sin^2\phi & (\cos\theta - 1)\sin\phi\cos\phi & \sin\theta\cos\phi \\ (\cos\theta - 1)\sin\phi\cos\phi & \cos\theta\sin^2\phi + \cos^2\phi & \sin\theta\sin\phi \\ -\sin\theta\cos\phi & \sin\theta\sin\phi & \cos\theta \end{bmatrix}. \tag{3.6}$$

Then the output beam is $\mathbf{E}_{\text{out}}(\theta,\phi) = \mathbf{T}\mathbf{E}_{\text{in}}(\theta,\phi)$. There is an immediate remark that must be made. Our incoming beam is paraxial in its propagation, and therefore the incoming waves are *transverse* electromagnetic waves. However, the transformed wave produced by refraction from an aplanatic objective produces a *longitudinal* component as well. The acquisition of the longitudinal component signifies our departure from paraxial propagation and reveals the mechanism by how light can be focused beyond the scalar diffraction limit - by acquiring a longitudinal component, the beam spot size w can be compressed to diameters that are comparable with the waves' wavelength, i.e. $w \simeq \lambda$.

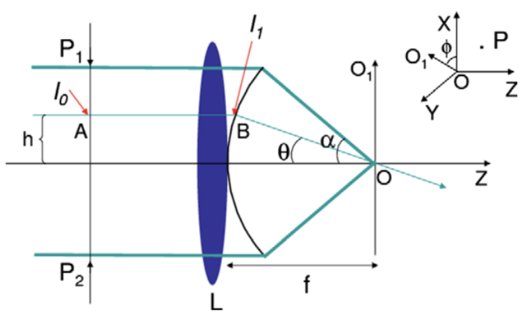

Figure 3.1: Diagram of the focusing of light from a spherical lens. The beam fills entirely the lens and rays traveling along the optic axis, shifted by a distance h from the optic axis satisfies the condition $h = f\sin\theta$ and are refracted radially towards the point $z = 0$. Adapted from reference [49].

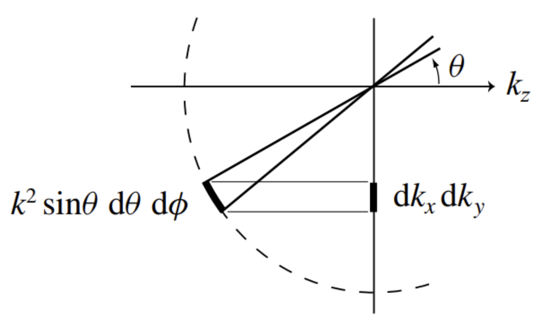

Figure 3.2: Diagram of the k-space of the beam when refracted by the lens and the geometry of going from k-space Cartesian coordinates to k-space spherical coordinates. Adapted from reference [48].

Having established the formalism for tightly focused fields, we now turn our attention to the focusing of Laguerre-Gaussian beams. Consider an x-polarized Laguerre-Gaussian beam that completely fills the aperture of a spherical lens and whose waist is sufficiently large that the lens lies within the beam's depth of focus. Under these conditions, the field distribution over the lens can be expressed in spherical coordinates as [51]

$$\mathrm{LG}_{0,\ell}(\theta,\phi) \propto \left(\frac{\sin\theta}{\sin\alpha}\right)^{|\ell|} \exp\left\{\left(-\frac{\sin^2\theta}{\sin^2\alpha}\right)\right\} \exp(i\ell\phi). \tag{3.7}$$

Here, we consider the lowest radial index of the LG mode, $p = 0$.

The x-polarization of the beam selects the first column of the matrix $\mathbf{T}$. The Richards-Wolf integral then becomes,

$$\sum_{n=-\infty}^{\infty} \int_0^{\alpha} \int_0^{2\pi} \quad \mathrm{LG}_{0,\ell}(\phi,\theta) e^{ikz\cos\theta} J_n(k\rho\sin\theta) e^{in(\varphi-\phi)} \sin\theta\sqrt{\cos\theta} \begin{bmatrix} \cos\theta\cos^2\phi + \sin^2\phi \\ (\cos\theta - 1)\sin\phi\cos\phi \\ -\sin\theta\cos\phi \end{bmatrix} d\phi d\theta, \tag{3.8}$$

where $J_n(.)$ denotes the Bessel function of the first kind of order n.

We will determine the OAM selection rules for tight-focusing (i.e., the values of n for which the integral is non-zero), as established in [22]. Observe that,

$$\int_0^{2\pi} e^{i(l-n)\phi} \cos^2\phi \, \mathrm{d}\phi = \begin{cases} \frac{\pi}{2}, & n = l \pm 2 \\ \pi, & n = l \\ 0, & \text{otherwise} \end{cases} \tag{3.9}$$

$$\int_0^{2\pi} e^{i(l-n)\phi} \sin^2\phi \, \mathrm{d}\phi = \begin{cases} -\dfrac{\pi}{2}, & n = l \pm 2 \\ \pi, & n = l \\ 0, & \text{otherwise} \end{cases} \tag{3.10}$$

$$\int_0^{2\pi} e^{i(l-n)\phi} \sin\phi\cos\phi \, \mathrm{d}\phi = \begin{cases} \pm\dfrac{\pi}{2i}, & n = l \pm 2 \\ 0, & \text{otherwise} \end{cases} \tag{3.11}$$

$$\int_0^{2\pi} e^{i(l-n)\phi} \cos\phi \, \mathrm{d}\phi = \begin{cases} \pi, & n = l \pm 1 \\ 0, & \text{otherwise} \end{cases} . \tag{3.12}$$

There are a few remarks that should be made: firstly, for an OAM state $|\ell\rangle$, we get non-conservation of OAM. This arises from coupling to the photon's spin degree of freedom, which will be examined more closely in the discussion to follow.

Having established the formalism describing the tight focusing of optical fields and explored the behavior of beams carrying spin and orbital angular momentum, we now turn our attention to the quantum regime. In particular, we investigate how tight focusing affects the spatial and angular-momentum properties of photon pairs generated via SPDC. As discussed in the previous chapters, SPDC is one of the most widely used sources of entangled photons, producing pairs whose spatial, momentum, polarization, and angular-momentum degrees of freedom exhibit strong quantum correlations. Since tight focusing is known to modify the structure of classical optical modes by introducing non-paraxial effects and coupling between different field components, it is natural to ask how these effects manifest themselves in correlated quantum states of light.

As a starting point, we consider the simplest and most commonly encountered configuration: a type I nonlinear BBO crystal pumped by a Gaussian beam. Under these conditions, the generated two-photon state can be expressed in terms of the transverse momentum correlations of the signal and idler photons. Neglecting the radial modes, the resulting biphoton state takes the following form

$$|\psi\rangle_{\text{in}} = \sum_{\ell=-\infty}^{\infty} C_l \, |\ell\rangle \, |-\ell\rangle \tag{3.13}$$

which is

$$\psi(\phi_i, \phi_s) = \sum_{\ell=-\infty}^{\infty} C_\ell \, e^{i\ell\phi_s} \, e^{-i\ell\phi_i} \tag{3.14}$$

in the real-space representation, i.e. $\langle \mathbf{r}_i, \mathbf{r}_s \, |\psi\rangle_{\text{in}}$. C_ℓ are the probability amplitudes of the OAM mode pairs. These coefficients are symmetric with respect to the sign of the orbital angular momentum, such that $C_\ell = C_{-\ell}$, and their distribution is determined by the pump and phase-matching properties of the SPDC process.

To understand how OAM is modified by tight focusing, it is useful to recall that the corresponding *selection rules* are determined entirely by the azimuthal structure of the field. In the present case, these rules emerge directly from the azimuthal integrals appearing in equations (3.9)–(3.12), which govern the coupling between the incoming and focused OAM modes. As discussed above for classical fields, the allowed mode transformations are dictated by angular-momentum conservation encoded in these integrals. The extension of this analysis to the biphoton state follows naturally. Since the Richards-Wolf formalism describes the action of a lens through a linear optical transformation, the focusing process acts independently on each photon of the pair. Mathematically, the focusing operation can therefore be represented as the tensor product of two single-photon integral operators. Consequently, the selection rules governing the tightly focused biphoton state are inherited directly from the corresponding single-photon transformations. This property greatly simplifies the analysis. Rather than evaluating a two-photon Richards–Wolf integral from first principles, one may first determine the tightly focused modes associated with each individual photon and then construct the focused biphoton state through their tensor product. The resulting two-photon field retains the quantum correlations established during the SPDC process, while simultaneously incorporating the non-paraxial mode mixing introduced by tight focusing. Accordingly, the focused biphoton state can be written as

$$\left(\widehat{\mathrm{RW}}_1 \otimes \widehat{\mathrm{RW}}_2\right)(|\psi_1\rangle_s \otimes |\psi_2\rangle_i) = (\widehat{\mathrm{RW}}_1 |\psi_1\rangle_s) \otimes (\widehat{\mathrm{RW}}_2 |\psi_2\rangle_i), \tag{3.15}$$

where $\widehat{\mathrm{RW}}$ indicates the action of tight focusing, given by the Richards-Wolf integral of the equation (3.8).

Now, our focused field for a single beam gives a vector field; therefore, the tensor product of two tightly-focused fields yields a rank-2 tensor field of the following form,

$$(\widehat{\mathrm{RW}}_1 |\psi_1\rangle_s) \otimes (\widehat{\mathrm{RW}}_2 |\psi_2\rangle_i) = \begin{bmatrix} \psi_{xx} & \psi_{xy} & \psi_{xz} \\ \psi_{yx} & \psi_{yy} & \psi_{yz} \\ \psi_{zx} & \psi_{zy} & \psi_{zz} \end{bmatrix}. \tag{3.16}$$

The square modulus of each entry gives the probability of detecting the two photons with either transverse or longitudinal polarization. For example, the entry ψ_{xy} would give you the probability of detecting the signal photon with x-polarization and the idler photon with y-polarization. From our work on the single beam tight-focusing we know that we have,

$$e^{i\ell\varphi_s} \mapsto \sum_{\Delta_s} A^{(\ell)}_{\Delta_s} e^{i(\ell+\Delta_s)\varphi_s} \tag{3.17}$$

$$e^{-i\ell\varphi_i} \mapsto \sum_{\Delta_i} B^{(-\ell)}_{\Delta_i} e^{i(-\ell+\Delta_i)\varphi_i} \tag{3.18}$$

where $\Delta = \ell - n \in \{0, \pm 1, \pm 2\}$, depending on whether we are dealing with transverse or longitudinal integrals. So, we have $m_s = \ell + \Delta_s$, and $m_i = -\ell + \Delta_i$, which gives the sum $m_s + m_i = \Delta_s + \Delta_i$. We may now write the total OAM selection rules for the tight focusing of a biphoton state,

$$\begin{aligned} m_s + m_i &\in \{0, \pm 2, \pm 4\} \rightarrow \text{Transverse selection rule} \\ m_s + m_i &\in \{\pm 1, \pm 3\} \rightarrow \text{Transverse-longitudinal selection rule} \\ m_s + m_i &\in \{0, \pm 2\} \rightarrow \text{Longitudinal selection rule} \end{aligned}$$

Observe that in the initial state, the total OAM is $J = \sum \ell = 0$, but after tight-focusing, the total OAM is non-zero again due to photon spin-orbit coupling. Moreover, since the initial state is a superposition of anti-correlated states, the tight-focusing of each of those modes couples them to "nearby" modes. To make this notion of "nearness" of modes a bit more precise, consider two modes given with indices $(-\ell, \ell)$, and $(-\ell - \Delta, \ell + \Delta)$ with $\Delta > 4$. Then the tightly focused fields of those two product states share no modes in common. This conclusion is pretty straightforward from The Great Lattice in figure 3.3.

The resulting broadening of the OAM spectrum in both the transverse and longitudinal components is a particularly intriguing consequence of tight focusing. Beyond its fundamental significance, this effect may have important implications for quantum imaging and quantum microscopy, where photon pairs are increasingly employed as probes of the spatial structure of unknown phase objects. In such applications, high numerical aperture systems are often required to achieve enhanced resolution, making non-paraxial effects unavoidable. Understanding how tight focusing alters the spatial and angular-momentum correlations of biphotons is therefore essential for accurately describing and exploiting these systems. It should be emphasized that the present analysis focuses primarily on OAM correlations and therefore captures only part of the underlying physics. As discussed in the previous chapter, the spatial structure of the SPDC state is considerably richer. Even for a Gaussian pump and within the thin crystal approximation, the generated biphoton state is generally correlated in both the azimuthal and radial degrees of freedom, as described by its Schmidt

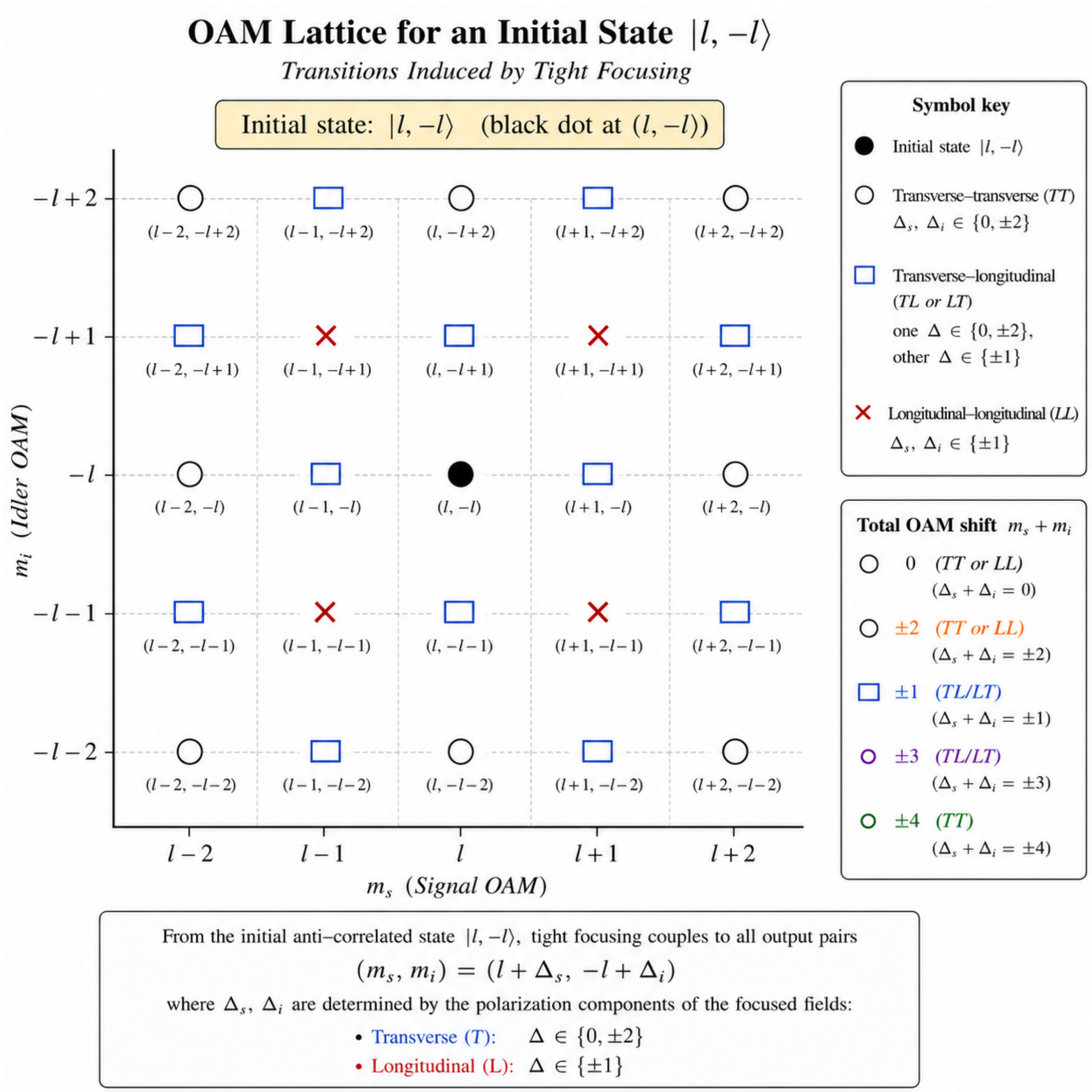

Figure 3.3: The Great Lattice depicts the possible OAM states that an SPDC photon pair may transition to, along with their indicated polarizations.

decomposition (it also possesses some non-negligible walk-off). The OAM basis considered here corresponds to the special case in which only the azimuthal structure is retained, while the radial mode index is neglected.

A more complete treatment of tight focusing must therefore include Laguerre-Gaussian modes with non-zero radial indices p. In this extended description, the lens not only induces coupling between neighboring OAM states through spin-orbit interactions, but may also generate coupling between radial modes. Such coupling is expected to depend on the detailed phase structure of the field, including the number and location of radial phase discontinuities, as well as on the numerical aperture of the focusing system. Consequently, tight focusing may reshape the biphoton state simultaneously in its azimuthal and radial degrees of freedom, leading to a much richer mode structure than that revealed by OAM correlations alone. Exploring these radial-mode effects remains an important direction for future work. A comprehensive understanding of the interplay between radial and azimuthal correlations in the non-paraxial regime could provide new insights into the structure of entangled photon pairs and may ultimately enable new approaches to high-dimensional quantum imaging, microscopy, and information processing.

4

Conclusion

In this thesis, we investigated the propagation and transformation of biphoton states generated through spontaneous parametric down-conversion (SPDC) in two distinct physical regimes. Our goal was to develop a deeper understanding of the spatial structure of entangled photon pairs and to explore how this structure evolves under propagation and strong optical manipulation. Together, these studies contribute to a broader effort to understand how quantum correlations behave in realistic optical systems and how they may be exploited in future imaging and microscopy applications. In Chapter 2, we examined the complete biphoton wavefunction generated by non-collinear type-I SPDC. Rather than relying on the double-Gaussian approximation that is frequently employed in the literature, we analyzed the full spatial structure of the biphoton state and its evolution during propagation. This approach revealed a variety of spatial correlations that are absent in simplified Gaussian models. Particular attention was devoted to the near-field regime, where the structure of biphoton correlations remains comparatively less explored than their far-field counterparts. Our analysis demonstrated that the near-field biphoton wavefunction contains a rich set of propagation-dependent features that encode information about the quantum state. These correlations evolve nontrivially as photons propagate and can provide valuable information for quantum state reconstruction. Furthermore, they play an important role in understanding diffraction and imaging through out-of-focus optical systems, where propagation effects cannot be neglected. These results highlight the importance of considering the full biphoton wavefunction when describing realistic quantum imaging scenarios and establish a framework for future investigations of propagation-dependent quantum measurements.

In Chapter 3, we moved beyond the paraxial approximation and investigated the behavior of structured quantum states in the non-paraxial regime. We first developed the formalism describing the tight focusing of vector optical fields and then extended this framework to biphoton states carrying orbital angular momentum (OAM). By applying the Richards-Wolf formalism to OAM-entangled photon pairs, we showed that tight focusing introduces spin-orbit interactions that fundamentally modify the angular momentum structure of the biphoton state. One of the central results of this work is the emergence of OAM selection rules associated with spin-to-orbit conversion. While the total OAM of the initial biphoton state may vanish, the focusing process couples spin and orbital angular momentum, broadening the distribution of OAM modes in the focal region. To describe these transitions, we introduced a geometric representation in the form of an OAM lattice, which provides an intuitive visualization of the allowed mode couplings and their relationships. This framework reveals how initially distinct OAM modes become interconnected through focusing-induced spin-orbit interactions and offers a powerful tool for understanding mode transformations in complex quantum optical systems. The resulting broadening of the OAM spectrum in both the transverse and longitudinal components is particularly significant. From a fundamental perspective, it demonstrates that tightly focused quantum fields cannot be fully understood within a paraxial description. From a practical perspective, these effects may play an important role in future quantum imaging and microscopy platforms, where high numerical aperture systems are essential for achieving high spatial resolution. In such systems, non-paraxial effects are not merely corrections but rather an intrinsic part of the imaging process. Consequently, understanding how tight focusing reshapes the spatial and angular momentum correlations of biphotons becomes crucial for accurately describing and exploiting these quantum states.

It is important to emphasize that the present treatment of tightly focused biphotons focused primarily on their OAM correlations. While this provides valuable insight into the role of spin-orbit coupling, it captures only part of the underlying structure of the SPDC state. Even under Gaussian pumping and within the thin-crystal approximation, SPDC generates correlations in both the azimuthal and radial degrees of freedom, as naturally described by the Schmidt decomposition of the biphoton wavefunction. The analysis presented in this thesis effectively corresponds to the special case in which the radial mode index is neglected, and only the azimuthal structure is retained.

A natural extension of this work is therefore to investigate the tight focusing of biphoton states expressed in the complete Laguerre-Gaussian basis, including modes with nonzero radial index p. In such a description, the focusing process may induce not only coupling between neighboring OAM states but also coupling between radial modes. Since radial modes are associated with the phase and intensity structure of the field in the transverse direction, their transformation is expected to depend sensitively on the optical system's numerical aperture and the detailed phase profile of the incoming field. The resulting interplay between radial and azimuthal correlations may generate a considerably richer entanglement structure than that revealed by OAM correlations alone.

The implications of these findings extend beyond the study of structured photons themselves. As quantum imaging techniques continue to mature, there is increasing interest in extending them from macroscopic imaging into the microscopic and nanoscopic regimes. Such a transition requires the integration of several areas of modern optics, including structured light, vectorial focusing, spin-orbit photonics, near-field optics, and high-dimensional quantum entanglement. The results presented in this thesis provide a theoretical foundation for this direction by clarifying how biphoton correlations evolve both during propagation and under strong focusing conditions. Several important questions naturally emerge from this work. For example, can entangled photons provide advantages over coherent illumination in scanning near-field optical microscopy? How are biphoton correlations modified by interaction with nanoscale scatterers or complex nanophotonic structures? Does spin-orbit conversion become enhanced or altered during such interactions? How is the OAM spectrum redistributed when an entangled photon pair encounters a subwavelength object? More broadly, can spin-orbit entanglement be harnessed to extract information that is inaccessible through classical illumination schemes?

Answering these questions will require a detailed understanding of the interplay between spatial correlations, spin-orbit coupling, and light-matter interactions at the nanoscale. The theoretical framework developed throughout this thesis represents a first step toward that goal. By combining a detailed description of the full biphoton wavefunction with a non-paraxial treatment of structured quantum states, this work opens new avenues for studying quantum light in regimes where diffraction, focusing, and entanglement become inseparable. As quantum technologies continue to advance, the ability to engineer and manipulate increasingly complex photonic states will become ever more important. The rich structure revealed here suggests that entangled photons possess untapped resources that remain largely unexplored, particularly in strongly focused and near-field environments. Exploring these resources may ultimately lead to new forms of quantum microscopy, enhanced imaging techniques, and novel methods for probing matter at the smallest scales. The path forward is challenging, but the opportunities are equally compelling, and the future of structured quantum light in microscopic imaging remains exceptionally promising.

References

[1] Max Planck. “On the theory of the energy distribution law of the normal spectrum”. In: *Verh. Deut. Phys. Ges* 2.237 (1900), pp. 237–245.

[2] Albert Einstein. “Über einen die Erzeugung und Verwandlung des Lichtes betreffenden heuristischen Gesichtspunkt”. In: *Annalen der Physik* (1905).

[3] Niels Bohr. “I. On the constitution of atoms and molecules”. In: *The London, Edinburgh, and Dublin Philosophical Magazine and Journal of Science* 26.151 (1913), pp. 1–25.

[4] A. Einstein, B. Podolsky and N. Rosen. “Can Quantum-Mechanical Description of Physical Reality Be Considered Complete?” In: *Physical Review* Volume 47 (1935).

[5] Andrew Zangwill. *Modern Electrodynamics*. Cambridge University Press, 2012.

[6] Robert W. Boyd. *Nonlinear Optics*. Fourth. Elseiver, 2020.

[7] Elijah Kannatey-Asibu Jr. *Principles of laser materials processing: developments and applications*. John Wiley & Sons, 2023.

[8] Eliot Bolduc et al. “Exact solution to simultaneous intensity and phase encryption with a single phase-only hologram”. In: *Optics letters* 38.18 (2013), pp. 3546–3549.

[9] Halina Rubinsztein-Dunlop et al. “Roadmap on structured light”. In: *Journal of optics* 19.1 (2017), p. 013001.

[10] Francesco Pampaloni and Jörg Enderlein. “Gaussian, hermite-gaussian, and laguerre-gaussian beams: A primer”. In: *arXiv preprint physics/0410021* (2004).

[11] Bahaa EA Saleh and Malvin Carl Teich. *Fundamentals of photonics, 2 volume set*. john Wiley & sons, 2019.

[12] John Frederick Nye and Michael Victor Berry. “Dislocations in wave trains”. In: *Proceedings of the Royal Society of London. A. Mathematical and Physical Sciences* 336.1605 (1974), pp. 165–190.

[13] Les Allen et al. “Orbital angular momentum of light and the transformation of Laguerre-Gaussian laser modes”. In: *Physical review A* 45.11 (1992), p. 8185.

[14] Jinwei Zeng et al. “Optical imaging using orbital angular momentum: interferometry, holography and microscopy”. In: *Journal of Lightwave Technology* 41.7 (2022), pp. 2025–2040.

[15] Lorenzo Marrucci. “The q-plate and its future”. In: *Journal of Nanophotonics* 7.1 (2013), pp. 078598–078598.

[16] Alison M Yao and Miles J Padgett. "Orbital angular momentum: origins, behavior and applications". In: *Advances in optics and photonics* 3.2 (2011), pp. 161–204.

[17] L Allen and MJ Padgett. "The Poynting vector in Laguerre–Gaussian beams and the interpretation of their angular momentum density". In: *Optics Communications* 184.1-4 (2000), pp. 67–71.

[18] Thomas Bauer et al. "Observation of optical polarization Möbius strips". In: *Science* 347.6225 (2015), pp. 964–966.

[19] Qi Zhu et al. "A review of optically induced rotation". In: *Frontiers of Information Technology & Electronic Engineering* 23.2 (2022), pp. 171–185.

[20] Fuquan Zhu et al. "Free-space optical communication link using perfect vortex beams carrying orbital angular momentum (OAM)". In: *Optics Communications* 396 (2017), pp. 50–57.

[21] Alan E Willner et al. "Optical communications using orbital angular momentum beams". In: *Advances in optics and photonics* 7.1 (2015), pp. 66–106.

[22] P Török and PRT Munro. "The use of Gauss-Laguerre vector beams in STED microscopy". In: *Optics express* 12.15 (2004), pp. 3605–3617.

[23] Albert Einstein et al. "On the motion of small particles suspended in liquids at rest required by the molecular-kinetic theory of heat". In: *Annalen der physik* 17.549-560 (1905), p. 208.

[24] Louis De Broglie. "Recherches sur la théorie des quanta". PhD thesis. Migration-université en cours d'affectation, 1924.

[25] Erwin Schrodinger. "An Undulatory Theory of the Mechanics of Atoms and Molecules". In: *The Physical Review* (1926).

[26] Sheldon Axler. *Linear Algebra Done Right*. Springer, 1996.

[27] Erwin Kreyszig. *Introductory Functional Analysis With Applications*. John Wiley & Sons, 1978.

[28] Teiko Heinsosaari and Mário Ziman. *The Mathematical Language of Quantum Theory*. Cambridge University Press, 2012.

[29] Ryszard Horodecki et al. "Quantum entanglement". In: *Reviews of modern physics* 81.2 (2009), pp. 865–942.

[30] Christopher C. Gerry and Peter L. Knight. *Introductory Quantum Optics*. Cambridge University Press, 2005.

[31] U. Fano. "Description of States In Quantum Mechanics by Density Matrix and Operator Techniques". In: *REviews of Modern Physics* volume 29.Number 1 (1957).

[32] Horatiu Nastase. *Quantum Mechanics: A Graduate Course*. Cambridge University Press, 2022.

[33] J.S. Bell. "On The Einstein-Podolski-Rosen Paradox". In: *Physics* 1 (1964).

[34] J.J. Sakurai and Jim Napolitano. *Modern Quantum Mechanics, second edition*. Cambridge University Press, 2017.

[35] Rodney Loudon. *The Quantum Theory of Light*. Third. Oxford Science Publications, 2000.

[36] Eugene Wigner. "On the quantum correction for thermodynamic equilibrium". In: *Physical review* 40.5 (1932), p. 749.

[37] S.P. Walborn, C.H.Monken, S. Pádua, P.H. Souto Ribeiro. "Spatial correlation in parametric down-conversion". In: *Physics Reports* (2010).

[38] S. Magnitskiy et al. "A SPDC Source of Entangled Photons and its Characterization". In: *Journal of Russian Laser Research* 36 (2015).

[39] SP Walborn, S Pádua, and CH Monken. "Conservation and entanglement of Hermite-Gaussian modes in parametric down-conversion". In: *Physical Review A—Atomic, Molecular, and Optical Physics* 71.5 (2005), p. 053812.

[40] SP Walborn et al. "Entanglement and conservation of orbital angular momentum in spontaneous parametric down-conversion". In: *Physical Review A* 69.2 (2004), p. 023811.

[41] Christophe Couteau. "Spontaneous parametric downconversion". In: *Contemporary Physics* (2018).

[42] Yu M Mikhailova, PA Volkov, and MV Fedorov. "Biphoton wave packets in parametric down-conversion: Spectral and temporal structure and degree of entanglement". In: *Physical Review A—Atomic, Molecular, and Optical Physics* 78.6 (2008), p. 062327.

[43] Chao Zhang et al. "Spontaneous parametric down-conversion sources for multiphoton experiments". In: *Advanced Quantum Technologies* 4.5 (2021), p. 2000132.

[44] AG da Costa Moura and CH Monken. "Einstein-Podolsky-Rosen correlations in spontaneous parametric down-conversion: Beyond the Gaussian approximation". In: *Physical Review A* 110.3 (2024), p. 033713.

[45] Felix Just et al. "Transverse entanglement of biphotons". In: *New Journal of Physics* 15.8 (2013), p. 083015.

[46] B. Richards and E. Wolf. "Electromagnetic diffraction in optical systems I. An integral representation of the image field". In: *Royal Society* (1959).

[47] B. Richards and E. Wolf. "Electromagnetic diffraction in optical systems II. Structure of the image in an aplanactic system". In: *Royal Society* (1959).

[48] Lukas Novotny and Bert Hecht. *Principles of Nano-Optics*. Cambridge University Press, 2006.

[49] BR Boruah and MAA Neil. "Focal field computation of an arbitrarily polarized beam using fast Fourier transforms". In: *Optics communications* 282.24 (2009), pp. 4660–4667.

[50] Eileen Otte, Kemal Tekce, and Cornelia Denz. "Tailored intensity landscapes by tight focusing of singular vector beams". In: *Optics express* 25.17 (2017), pp. 20194–20201.

[51] Manuel Francisco Ferrer Garcia. "Structuring Light: From knots to geometrical phases". PhD thesis. Université d'Ottawa— University of Ottawa, 2024.